

LINKING GEOMORPHIC PROCESS AND LANDSCAPE FORM: TOPOGRAPHIC
ANALYSIS, ANALOG EXPERIMENTS, AND NUMERICAL MODELING

by

KRISTIN ELIZABETH SWEENEY

A DISSERTATION

Presented to the Department of Geological Sciences
and the Graduate School of the University of Oregon
in partial fulfillment of the requirements
for the degree of
Doctor of Philosophy

September 2015

DISSERTATION APPROVAL PAGE

Student: Kristin Elizabeth Sweeney

Title: Linking Geomorphic Process and Landscape Form: Topographic Analysis, Analog Experiments, and Numerical Modeling

This dissertation has been accepted and approved in partial fulfillment of the requirements for the Doctor of Philosophy degree in the Department of Geological Sciences by:

Joshua J. Roering	Chairperson
Rebecca Dorsey	Core Member
Alan W. Rempel	Core Member
Mark Fonstad	Institutional Representative

and

Scott L. Pratt	Dean of the Graduate School
----------------	-----------------------------

Original approval signatures are on file with the University of Oregon Graduate School.

Degree awarded September 2015

© 2015 Kristin Elizabeth Sweeney

DISSERTATION ABSTRACT

Kristin Elizabeth Sweeney

Doctor of Philosophy

Department of Geological Sciences

September 2015

Title: Linking Geomorphic Process and Landscape Form: Topographic Analysis, Analog Experiments, and Numerical Modeling

Erosive landscapes are formed from the amalgamation of individual sediment transport over space and time. Though sediment transport is readily observable at the grain and event scales, determining how these events conspire to form hillslope, rivers, and mountain ranges requires transcending considerable gaps in spatial and temporal scale. In this dissertation, I use a broad range of methods across a diverse suite of landscapes to quantify how geomorphic processes dictate landscape form.

In Chapter II, I assess the magnitude of local variability in erosion in the Oregon Coast Range using the residence time of hilltop soils as a proxy for local erosion rate. I develop a new technique for measuring the soil weathering extent using visible–near - infrared spectroscopy. My results from this chapter indicate that the frequency and spatial distribution of hillslope disturbances, in this case tree throw, are primary controls on the magnitude of erosional variability. In Chapter III I take a different approach to tackling process-form linkages in eroding landscapes by systematically changing the dominant erosion process in a meter-scale laboratory landscape and quantifying the resulting topography. This approach is in contrast to most geomorphic investigations, which fit process models to static natural topography, ignoring the potential for changing process

rates through time or the effect of initial conditions on landscape evolution. The steady-state topography of my experiments confirms numerical predictions that the drainage density of mountain ranges depends on the efficiency of hillslope transport relative to the efficiency of channel incision. Finally, in Chapter IV, I present my investigation of the early stages of landscape evolution on a Holocene lava flow in the Oregon High Cascades that has been incised by a fluvial channel. Here, I use lidar measurements, alluvial stratigraphy, and numerical modeling to constrain the type and magnitudes of channel-forming events. In contrast to past work in flood basalts, which point to the dominant role of megafloods in forming channels, my results demonstrate that both large outburst floods and smaller annual snowmelt flows are responsible for channel incision.

This dissertation includes previously published and co-authored material.

CURRICULUM VITAE

NAME OF AUTHOR: Kristin Elizabeth Sweeney

GRADUATE AND UNDERGRADUATE SCHOOLS ATTENDED:

University of Oregon, Eugene, OR
Carleton College, Northfield, MN

DEGREES AWARDED:

Doctor of Philosophy, Geological Sciences, 2015, University of Oregon
Bachelor of Arts, Geology, 2009, Carleton College

AREAS OF SPECIAL INTEREST:

Geomorphology

PROFESSIONAL EXPERIENCE:

Graduate Teaching and Research Fellow, University of Oregon, 2010 - 2015
Research Assistant, St. Anthony Falls Laboratory, U. of Minnesota, 2009 – 2010
Teaching Assistant, Carleton College, 2008 - 2009

GRANTS, AWARDS, AND HONORS:

Graduate Research Grant, Mazamas, 2014

National Center for Airborne Laser Mapping Seed Grant, 2012

NSF Graduate Research Fellowship, Honorable Mention, 2012

Thayer Scholarship, University of Oregon, 2011, 2012, 2014

Distinction in Senior Thesis, Carleton College, 2009

Duncan Stewart Geology Fellowship, Carleton College, 2009

Inducted to Phi Beta Kappa, 2009

PUBLICATIONS:

- Sweeney, K.E., J.J. Roering, and C. Ellis, (2015), Experimental evidence for hillslope control of landscape scale, *Science*, v. 349 (6243), 51-53. doi: 10.1126/science.aab0017
- Pelletier, J., K.E. Sweeney, J.J. Roering, and N. Finnegan, (2015), Controls on the geometry of potholes in bedrock channels, *Geophysical Research Letters*, 42 (3), 797 – 803. doi: 10.1002/2014GL062900
- Roering, J.J., B.H. Mackey, J.A. Marshall, K.E. Sweeney, A.M. Booth, N. Deligne, A.M. Handwerker, and C. Cerovski-Darriau, (2013), ‘You are HERE’: Connecting the dots with airborne lidar for geomorphic fieldwork, *Geomorphology*, 2012 Binghamton Symposium, “The Field Tradition in Geomorphology”, doi:10.10106/j.geomorph.2013.04.009.
- Sweeney, K.E., J.J. Roering, P. Almond, and T. Reckling, (2012), How steady are ‘steady-state’ landscapes? Using soil spectroscopy to quantify erosional variability, *Geology*, v. 40, p. 807-810.
- Frankel, K.L., K.W. Wegmann, A. Bayasgalan, R.J. Carson, N.E. Bader, T. Adiya, E. Bolor, C.C. Durfey, J. Otgonkhuu, J. Sprajcar, K.E. Sweeney, R.T. Walker, T.L. Marsteller, L. Gregory, 2010, Late Pleistocene slip rate of the Hoh Serh – Tsagaan Salaa fault system, Mongolian Altai and intracontinental deformation in central Asia, *Geophysical Journal International*, v. 183, 1134-1150

ACKNOWLEDGMENTS

Thanks to my advisor Josh Roering for teaching me how to ask tractable questions and make people care about those questions, and for providing evidence that the qualities of a great scientist, a great teacher, and a decent human being are not mutually exclusive. I thank my committee members Rebeca Dorsey, Alan Rempel, and Mark Fonstad for giving me invaluable feedback on my work over the last five years with promptness and good humor.

The St. Anthony Falls Laboratory in Minneapolis has fundamentally shaped my scientific career. In particular, Chapter III would not have been possible without: Chris Ellis, Jeff Marr, Dick Christopher, the SAFL technical staff, Arvind Singh, and Efi Fofoula-Georgiou. Thanks also to the Christopherson family for understanding my nontraditional schedule while I ran experiments and slept in their attic, and to my collaborators Peter Almond, Till Reckling, Jon Pelletier, and Noah Finnegan for their scientific input and generosity.

This success of this work depended heavily on my friends in the UO geology department, the Eugene frisbee community, and elsewhere, particularly: Corina Cerovski-Darriau, Jill Marshall, Ashley Streig, Scott Maguffin, Kristina Walowski, Natalia Deligne, George Roth, Brendan Murphy, the ladies of Riverview and the Quintron, and Christopher Burke. I am eternally grateful to my family for encouraging my lifelong interest in the natural world, especially their tolerance of dirt tracked through the house, plants growing on windowsills and molding in cupboards, and public spaces full of worms, seashells, and detritus of all varieties. Thanks to my parents, Peter Sweeney and

Julie Keil, for supporting my education emotionally and materially and to my sister Caitlin Sweeney, for being both a reliable source of advice and a paragon of style.

This work was funded by National Science Foundation EAR grant 1252177 to Josh Roering and Chris Ellis, a graduate research grant from the Mazamas, and a National Center for Airborne Laser Mapping Seed Grant. I also received travel funds, research support, and field equipment from the University of Oregon Department of Geological Sciences.

TABLE OF CONTENTS

Chapter	Page
I. INTRODUCTION	1
II. HOW STEADY ARE STEADY-STATE LANDSCAPES? USING VISIBLE – NEAR-INFRAFRED SPECTROSCOPY TO QUANTIFY EROSIONAL VARIABILITY	5
1. Introduction.....	5
2. Study Site	7
3. Soil Weathering and Residence Time.....	10
4. Spectral Analysis and Calibration.....	11
5. Residence Time of Hilltop Soils and Erosional Variability.....	12
6. Discussion and Conclusions	16
7. Bridge.....	16
III. EXPERIMENTAL EVIDENCE FOR HILLSLOPE CONTROL OF LANDSCAPE SCALE	18
1. Bridge.....	28
IV. RAPID FLUVIAL INCISION OF A LATE HOLOCENE LAVA FLOW: INSIGHTS FROM LIDAR, ALLUVIAL STRATIGRAPHY, AND NUMERICAL MODELING	29
1. What Sets the Pace of Fluvial Incision in Volcanic Landscapes?	29
2. Approach and Scope	31
3. Volcanic and Glacial Setting	35
4. Methods.....	37

Chapter	Page
4.1. Measuring Channel Morphology and Incision	37
4.2. Alluvial Stratigraphy and Radiocarbon Sampling	38
5. Field Evidence for Incision Mechanisms and Timing	39
5.1. Gorge Morphology: Pre-incision Topography and Sediment Provenance	40
5.2. Alluvial Morphology: Implications for Sediment Transport	40
5.3. Alluvial Stratigraphy	41
5.4. Hydrologic Regime	43
6. Modeling Philosophy: Assessing the Driving Forces of Incision	43
7. Model Formulation and Procedure	46
7.1. Assumptions and Parameter Constraints	46
7.1.1. Discharge and Shear Stress	46
7.1.2. Grain Size	47
7.1.3. Sediment Supply	48
7.2. Mechanistic Modeling of Bedrock Abrasion	48
7.3. Governing Equations	49
7.4. Modeling Procedure	50
8. Combined Role of Large Floods and Annual Discharge	51
9. Discussions/Conclusions	54
9.1. Incision Mechanisms	54
9.2. Evolution of Temperate Volcanic Landscapes	55

Chapter	Page
APPENDICES	56
A. SUPPLEMENTAL INFORMATION FOR CHAPTER II.....	56
B. SUPPLEMENTAL INFORMATION FOR CHAPTER III	58
C. SUPPLEMENTAL INFORMATION FOR CHAPTER IV.....	66
REFERENCES CITED.....	72

LIST OF FIGURES

Figure	Page
1. Study watersheds with sample locations and mapped igneous dikes	9
2. Spectral analysis of terrace chronosequence.....	13
3. PDF of soil residence times	14
4. Characteristic morphology of eroding landscapes	19
5. Experimental setup.....	22
6. Steady-state topography and hillslope morphology.....	24
7. Effect of landscape Péclet number on landscape scale.....	27
8. Regional setting	32
9. Geologic setting of Collier lava flow.....	33
10. Channel morphology and topography.....	34
11. Field expression of channel morphology.....	36
12. Slope of alluvium.....	38
13. Pit stratigraphy.....	39
14. Radiocarbon dating of alluvial deposits.....	42
15. Correlation between slope and incision	44
16. Model behavior.....	52
17. Modeled incision rates and inferred active incision time	53

CHAPTER I

INTRODUCTION

Landscapes are formed by the temporal and spatial integration of sediment transport. Many of these processes can be observed and quantified at the event scale, from single grains moving through a laboratory river to kilometer-scale debris flows and flash floods. Similarly, advances in airborne light detection and radar (lidar) has enabled increasing precision in the measurement of natural topography, allowing us to develop metrics describing landscape form. Despite these advances, there is a fundamental gap in space and time scale between sediment transport observations and measurements of landscape form. This gap leads to critical questions about the link between sediment transport processes and landscape evolution: How variable are geomorphic processes over time and space? How should we represent this variability in models of landscape evolution? What range of event magnitudes contribute to long-term erosion? In this dissertation I address some of these questions in the Oregon Coast Range, a laboratory-scale landscape, and in the High Cascades of Oregon. I use a broad range of techniques to do this, including spectroscopy, analysis of high-resolution topography, analog laboratory experiments, and numerical modeling.

Chapter II was co-authored with Joshua Roering (University of Oregon), Peter Almond (Lincoln University, New Zealand), and Till Reckling, and published in the journal *Geology* in September 2012.

Long-term watershed erosion rates are typically reported as a single spatially-averaged value for each watershed, mostly owing to the expense of analyzing cosmogenic nuclide concentration in stream sediment (the typical geochemical technique

for measuring erosion rate). In Chapter II, I quantify the spatial variability in erosion rate within a single watershed and attempt to discern the root cause of this variability. Based on an assumption of flux steady-state, such that erosion balances rock uplift, the residence time of hilltop soils should be inversely related to local erosion rate. Working in Hoffman Creek watershed in the Oregon Coast Range, I develop a method for measuring the extent of soil weathering with visible–near-infrared spectroscopy and convert these measurements to soil residence time using a previously established chronosequence. The standard deviation of soil residence times for the watershed (~10,000 years) corresponds to the approximate time for complete turnover of a Douglas fir forest, suggesting that tree throw processes control the spatial variability of erosion. I also show that the distribution of soil residence times in Hoffman Creek, a steadily eroding watershed, is a different shape than the residence time distribution in Kentucky Creek, which is undergoing transient divide migration due to a local lithologic control. This finding may help future assessments of landscape transience, both in the Oregon Coast Range and elsewhere.

Chapter III was co-authored by Joshua Roering (University of Oregon) and Christopher Ellis (University of Minnesota) and published in *Science* in July, 2015.

Numerical models predict that the spacing of ridges and valleys in eroding landscape depends on the efficiency of hillslope diffusion relative to channel incision, expressed as a landscape Peclet number (Perron et al., 2009). However, owing to the slow and episodic nature of erosion, tests of this model are limited to fitting process parameters to static natural topography. For my third chapter, I designed a set of five analog experiments that systematically varied the landscape Peclet number and measured

the steady-state topography that resulted. Hillslope diffusion in the experiments was generated by large impacting raindrops and channel incision was driven by finer-scale rainfall from a set of misters. The steady-state topography of the experiments confirms the prediction of numerical models: landscapes dominated by hillslope transport are smoother and have more widely spaced valleys, while channel-dominated landscapes are highly dissected.

Chapter IV was co-authored by Joshua Roering (University of Oregon) and is in preparation for submission to the *Geological Society of America Bulletin*.

Volcanic eruptions profoundly disturb landscapes, in many cases obliterating the organization of the pre-eruption topography. Hence, volcanic landscapes present a unique opportunity to quantify the early stages of landscape evolution and geomorphic processes. Past workers have demonstrated the importance of megaflood events for forming channels in columnar basalt, but it is not clear how these events might shape landscapes where vertical jointing is not present. In Chapter IV, I examine the rapid fluvial incision of Collier lava flow, a Holocene flow in the High Cascades where a channel has incised up to 8 m into the coherent core of the flow. The unaltered surface of the flow enables us to interpolate a pre-incision surface and calculate local incision along the length of the channel. There is evidence that both moderate annual snowmelt flows and large outburst floods from nearby Collier Glacier occur in this channel. To determine the geomorphic importance of these two classes of events, I modeled instantaneous incision rates in the channel with a mechanistic formulation for fluvial abrasion, using measured topography and field observations to constrain model parameters. The results

from this work show that in order to explain the incision we observe, both outburst floods and annual snowmelt runoff must contribute to channel incision.

CHAPTER II

HOW STEADY ARE STEADY-STATE LANDSCAPES? USING VISIBLE – NEAR-INFRARED SPECTROSCOPY TO QUANTIFY EROSIONAL VARIABILITY

This chapter was published in *Geology* in September, 2012. I was the lead author on the paper, developing the methodology, analyzing the data, and writing. My co-authors, Joshua Roering (University of Oregon) and Peter Almond (Lincoln University), served as advisors, helping with data interpretation and manuscript editing. The final author, Till Reckling, collected many of the samples used in the paper and performed an earlier analysis of soil color that led us to idea of the spectroscopic method.

1. Introduction

Topographic steady state, the assumption of constant landscape form through the perfect balance of erosion and rock uplift, is the theoretical endpoint of landscape adjustment to constant climatic and tectonic forcing (Fernandes and Dietrich, 1997; Willett and Brandon, 2002). Assumptions of topographic steady state in geomorphology simplify the calibration and testing of sediment transport equations. Furthermore, numerical models of landscape response to perturbations in climate and tectonics often use steady-state topography as the initial condition (Rinaldo et al., 1995) and experimental models are generally run until they achieve some approximation of steady-state topography (Lague, 2003). Erosion data derived from stream sediment in the Oregon Coast Range (OCR) and other settings suggest topographic steady state may exist in some natural landscapes but the scale at which this equilibrium applies is poorly defined (Reneau and Dietrich, 1991; Meigs et al., 1999)

Strict steady-state denudation does not necessarily hold in numerical and experimental landscapes, even under constant forcing. For example, previous work has documented frequent divide migration and drainage reorganization in an experimental watershed (Hasbargen and Paola, 2000). Pelletier (2004) created similar behavior in a numerical model by distributing flow with a weighted drainage area algorithm rather than one driven by steepest descent. These findings give rise to the question: how much variability can be expected in steady natural landscapes and how can such local unsteadiness be measured?

Advances in cosmogenic radionuclide (CRN) techniques have enabled increasingly precise measurements of soil production and erosion rates and corresponding inferences about landscape processes (e.g., Riebe et al., 2004). Although CRNs are a powerful tool, the high cost of processing limits information to a handful of samples for a given watershed or catchment-wide averages, often insufficient to quantify local erosional variability.

If soil-forming factors other than time are held constant, the rate of erosion in soil-mantled landscapes can be inferred from soil features (Birkeland, 1999). The progression of chemical weathering, for example, can manifest over time as monotonic losses of primary minerals or increases in pedogenic minerals. During weathering, accumulation of the secondary Fe mineral hematite gives older soils a distinctive red color (McFadden and Hendricks, 1985); this signature can be captured analytically with visible–near-infrared (visNIR) spectroscopy (Scheinost, 1998; Viscarra Rossel et al., 2010). By calibrating a spectroscopy-based weathering function in a given landscape, we can estimate the soil residence time, defined as the average transit time of particles in the

soil column, and thus quantify relative variations in erosion rate (Almond et al., 2007; Mudd and Yoo, 2010).

In this study, we use visNIR soil spectroscopy to quantify the statistics of erosional variability at the local and watershed scale. We collected 137 samples from hilltops in two watersheds with different erosional settings in the OCR, a humid soil-mantled landscape with relatively homogeneous lithology often considered the ‘textbook case’ for topographic steady state (Reneau and Dietrich, 1991). We calibrate our weathering function with data from a chronosequence of alluvial terraces along the Siuslaw River, OR (Almond et al., 2007) and show that the visNIR spectrum changes systematically with terrace age. Our findings demonstrate that erosional variability in uniformly eroding landscapes can reflect sediment transport processes and that soil data can be used to document catchment dynamics over geologic timescales.

2. Study Site

The humid, steep, soil-mantled landscape of the OCR is underlain by the Tyee Formation, a relatively undeformed turbidite sandstone (Heller and Dickinson, 1985). Igneous dikes crop out locally, often forming the highest elevation ridgelines in the region. Most of the OCR is covered in Douglas fir forest and has annual rainfall between 1 and 2 m. In upland catchments, sediment transport is dominated by shallow landslides and debris flows in valley networks (Stock and Dietrich, 2003) and bioturbation and small soil slips on hillslopes (Gabet and Mudd, 2010). Reneau and Dietrich (1991) used colluvial hollows in the OCR to measure bedrock exfoliation rates of 0.09 mm/yr, similar to their basin-wide denudation rates of 0.05–0.08 mm/yr. These rates are comparable to soil production estimates of 0.02–0.16 mm/yr (Heimsath et al., 2001) and catchment-

averaged erosion rates of 0.137 mm/yr generated by CRNs (Bierman, 2001). Measurements of uplift are variable (0.06 mm/yr to 0.2 mm/yr) due to local structural controls, but are grossly similar (Personius, 1995). These data suggest that the OCR may be in approximate flux steady state such that rock uplift balances erosion. Furthermore, the uniform ridge-valley topography that characterizes much of the OCR has been presented as evidence for topographic steady state, whereby the smoothing effect of hillslope erosion is balanced by landscape roughening via valley-forming processes (Perron et al., 2009). The time and spatial scales over which the steady-state approximation applies have not been rigorously characterized for the OCR, although previous work acknowledges that local variability around steady state likely arises from the stochasticity of hillslope processes, and, more broadly, from knickpoints that modulate local baselevel (Heimsath et al., 2001; Stock and Dietrich, 2003; Roering et al., 2010).

Here we consider erosional patterns in two watersheds in the OCR (Fig. 1), selected to compare the erosional dynamics of ‘adjusted’ (or approximately steady state) and ‘pinned’ or slowly eroding landscapes. Hoffman Creek (HC) drains directly into the Siuslaw River and contains no mapped lithologic contacts. The topography is steep (mean slope 60%) and highly dissected with evenly-spaced ridge/valley sequences. In contrast, the North Fork of the Smith River (NFSR) is ‘pinned’ by a ~100 m wide gabbroic dike that forms a 70 m high knickpoint. This elevated local baselevel is reflected by gentler slopes (mean: 39%) and broad alluvial valleys upstream of the knickpoint (Fig. 1), suggesting that this catchment is eroding more slowly.

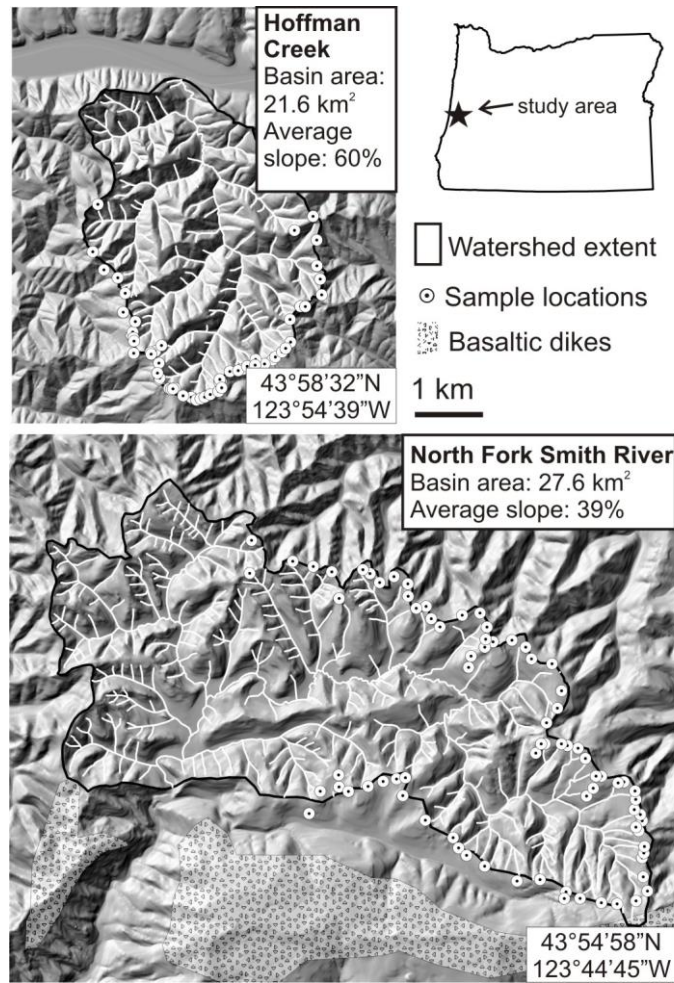


Figure 1. Study watersheds with sample locations and mapped igneous dikes. Latitude/longitude labels are for the bottom corner of each watershed map. Oregon state outline shows geographic location of study area.

Our weathering function is calibrated with data from a soil chronosequence of seven alluvial terraces (T1 – T7) on the Siuslaw River, previously described by Almond et al. (2007). The chronosequence lies within the same precipitation regime as our two study watersheds and is also underlain by the Tye Formation. Gravels along the strath/alluvium interface of these terraces are geochemically indistinguishable from unweathered bedrock (Almond et al., unpublished data). Radiocarbon dates from T1 and T2 yield an estimated incision rate of 0.15 mm/yr on the Siuslaw River, similar to average erosion estimates for the OCR. This rate and terrace surveys allowed us to

extrapolate ages for T3 – T7, assuming that incision has been broadly consistent for the past 1000 k.y. (Almond, et al., 2007).

3. Soil Weathering and Residence Time

In the time between detachment from bedrock and delivery to the valley network, soil particles are subject to chemical weathering. The extent and manner of this alteration depend on parent material, biology, topography, climate, and time (Jenny, 1941). By collecting samples in the Tye Formation from hilltops (i.e., sites with ~0 slope) in a small geographic area, we can assume that soil forming factors are similar at sampling locations and that variations in weathering between samples can be attributed to the difference in time that particles spend in the soil column.

Using measurements of soil weathering to quantify landscape dynamics requires that we define the relationship between weathering extent and erosion rate (e.g., Mudd and Yoo, 2010). Residence time, the average transit time of a particle in the soil column,

is a measure of the time that soils are exposed to weathering and is thus inversely related to erosion rate. In other words, soil residence time can be directly estimated from soil properties and yield information about erosional patterns in the landscape.

For a hillslope with steady, uniform erosion, residence time τ depends on mobile soil

depth h , erosion rate E , and soil-bedrock density contrast $\frac{\rho_r}{\rho_s}$ (Almond et al., 2007):

$$\tau = \frac{h}{E} \frac{\rho_r}{\rho_s} \quad (1)$$

To link residence time and the degree of soil weathering, we follow the methodology of Almond et al. (2007) and define an exponential weathering function for soil particles

$$W(t) = W_0 + K(1 - e^{-\lambda t}) \quad (2)$$

where W_0 is the weathering state of rock entering the mobile layer, K and λ are fit parameters describing how the state of weathering varies over time, and t is the transit time. The extent of weathering for a given soil profile is equal to the average weathering extent of the particles comprising it. To average weathering in the soil column, we integrate Equation 2 along the hillslope and obtain the relationship between residence time τ and weathering extent W , assuming that bedrock enters the soil column with a constant weathering signature W_0 :

$$\tau = \frac{W - W_0}{\lambda(K - [W - W_0])} \quad (3)$$

Fitting Equation 2 to our chronosequence data provides parameter estimates such that we can use Equation 3 to calculate soil residence times from the weathering extent of hilltop soils in the HC and NFSR catchments. These soil residence times can then be used to infer local erosion rates from Equation 1.

We use hematite content as a proxy for the degree of soil weathering because it is well-expressed in soil color. The release of iron cations during weathering produces either goethite or hematite, depending on pedogenic conditions (Schwertmann and Taylor, 1989), and the low soil moisture of OCR hilltop soils favor hematite production (Patching, 1987). Sampling the B horizon standardizes the hematite signal in our spectra, as the B horizon is less vulnerable to frequent physical disturbance than the upper portion of the soil column and is the preferred zone of pedogenic iron accumulation (Birkeland, 1999).

4. Spectral Analysis and Calibration

VisNIR reflectance spectroscopy measures the reflectance (R) of a sample relative to a white standard at wavelengths of 350 to 1000 nm. The magnitude of the spectrum is

affected by the distance from the sensor and the grain size/roughness of the material, while the mineral composition of the sample controls the spectrum shape. Characteristic peaks (seen as dips in reflectance spectra) are due to mineral electron transitions. Previous work has shown that hematite has a characteristic peak at 880 nm (Scheinost, 1998).

We collected samples from the B horizons of T1-T7, typically at 40 - 50 cm depth. Each sample was dried, sieved to 63 μ , and packed in a petri dish to provide an even surface for spectroscopic analysis. VisNIR spectra from the seven terraces of the chronosequence display a characteristic shape with some important differences (Fig. 2A). Typical visNIR analysis normalizes spectra to remove background slopes that may obscure the signal (Clark and Roush, 1984). Because the hematite peak in our data is readily apparent without normalization, we analyzed raw spectra. The slope of the spectra between 790 nm and 880 nm (shaded box in Fig. 2A) is a measure of the relative magnitude of the 880 nm hematite peak.

The chronosequence soils show a systematic trend of reddening (Fig. 2B). Spectral slopes between 790 and 880 nm decrease with terrace age from 0.04 R/nm to ~0.05 R/nm (Fig. 2C). Using Equation 2, the best fit model for the chronosequence measurements ($r^2 = 0.97$) has $W_0 = 0.0544 (\pm 0.009)$, $K = -0.0981 (\pm 0.009)$, and $\lambda = 0.0120 (\pm 0.003)$ (Fig. 2C).

5. Residence Time of Hilltop Soils and Erosional Variability

We took samples from the B horizons of 137 hilltop locations, 59 in the morphologically uniform HC and 78 in the gentle uplands of NFSR. To calculate residence times from spectral measurements, we used Equation 3 fit with the

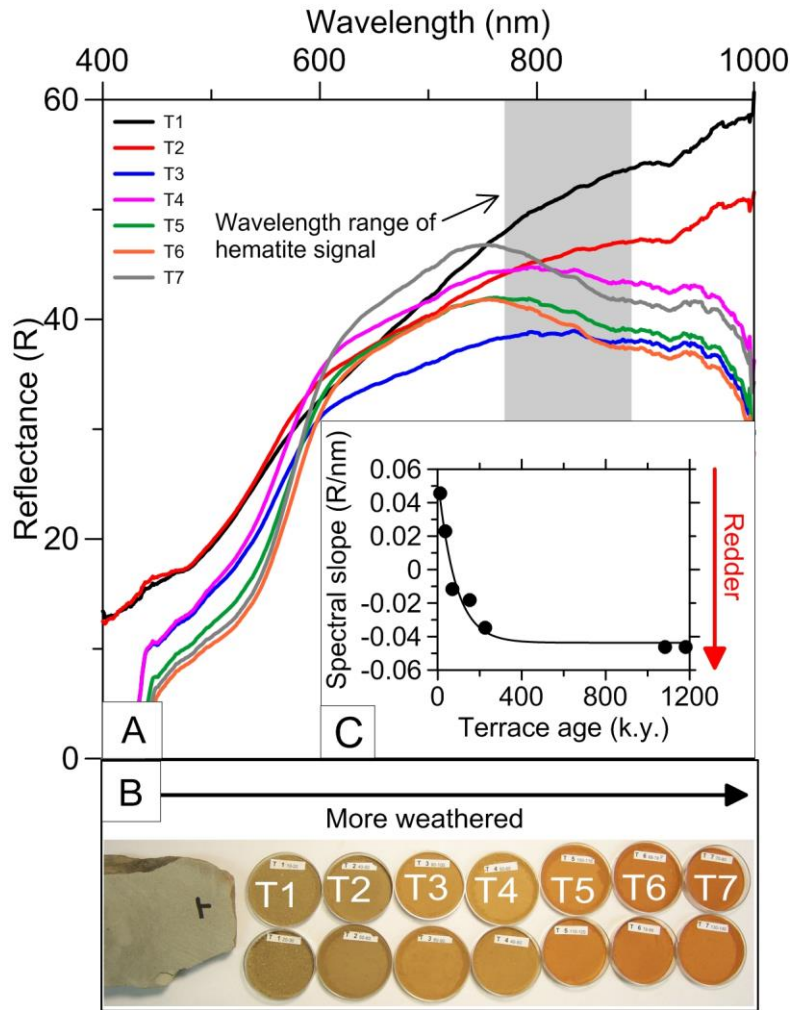


Figure 2. Spectral analysis of terrace chronosequence. (a) Raw spectra from chronosequence. Shaded gray box highlights section of spectra used for analysis; notice that the slopes of the spectra in this interval decrease with terrace age. (b) Samples from chronosequence showing reddening with age. Rock is fresh bedrock from the Tye formation. (c) Spectral slopes (dots) fit by exponential weathering function (line; Equation 2), with $W_0 = -0.0544$, $K = 0.0981$, and $\lambda = 0.0120$ ($r^2 = 0.97$). Error bars are smaller than symbol radius.

chronosequence parameters (solid line in Fig. 2C). Residence times in both watersheds can be described by skewed distributions, which have been log-transformed to emphasize the distinctive shapes of the two distributions (Fig. 3). Mean soil residence time in HC is 18.8 k.y. (+ 31.2/-11.8 k.y.), whereas the mean residence time for NFSR is 72.9 k.y. (+165.6/-50.6 k.y.).

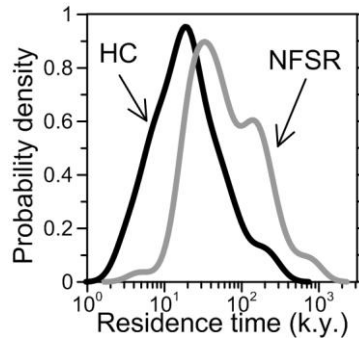


Figure 3. PDF of soil residence times for HC (black) and NFSR (gray). Uncertainty from Gaussian error propagation is 30%–40%. PDF smoothing window is 1.5 k.y. Mean and standard deviation calculated from log-transformed distributions.

The distribution of residence times for HC, our ‘adjusted’ watershed, shows that soil residence times exhibit substantial variation, suggesting that steady, uniform erosion does not hold in real landscapes. The semi-variogram of HC residence times (Fig. A1; see Appendix A for all supplemental figures for this chapter) shows that at lags > 100 m our measurements are spatially uncorrelated, implying that the process dominating erosional variability occurs at smaller scales. Despite local variability, the mean soil residence time for HC agrees with the expected value from Equation 1 using previously estimated parameters for the OCR ($h = 0.5 - 1.0$ m, $E = 0.1$ mm/yr, and $\frac{\rho_r}{\rho_s} = 2.0$; Heimsath et al., 2001), suggesting that the approximation of steady, uniform erosion is relevant at the catchment scale.

We hypothesize that local erosional variability in the HC study site results from the stochasticity of hillslope processes related to tree root activity, including rootwad turnover. Previous authors have found that root comminution of bedrock and tree throw disturbance are important components of soil production and sediment transport in the OCR (Gabet and Mudd, 2010; Roering et al., 2010). Tree throw results in a patchwork of

soil disturbance history, and, by extension, local variations in soil production and erosion rate (Norton, 1989). Our interpretation assumes that rootwad turnover extricates relatively unweathered bedrock, which is supported by previous observations (Roering et al., 2010). The similarity between Roering et al.'s (2010) estimate of the timescale of total landscape turnover via tree throw (15 – 20 k.y.) and the standard deviation for the HC residence time distribution (+ 31.2/-11.8 k.y.) suggests that bioturbation may control the magnitude of residence time variability in the HC watershed. If hillslope transport regimes in soil-mantled landscapes are dominated by physical disturbance (Gabet, 2000; Roering et al., 2010), we postulate that local erosional variability in 'steady' landscapes reflects the scale of soil production and transport mechanisms.

By contrast, a lithologic baselevel control may be responsible for the significant proportion of long residence time soils along NFSR hilltops. The deviation of the weakly bimodal NFSR residence time distribution from the log-normal shape of the HC data suggests that the hilltop soils of NFSR may record an imbalance between local controls and regional baselevel lowering driven by rock uplift. Past work suggests that persistent differential erosion across divides may result in ridge migration (Mudd and Furbish, 2005). This mechanism may drive south-directed divide migration along the northern edge of the NFSR catchment (Fig. 1; Fig. A2). We speculate that the smaller and older peak in the distribution (at 200 k.y.) reflects slower hillslope erosion set by the baselevel of the gabbroic dike downstream, while the larger peak (~30 k.y.) derives from the impingement of steep, highly dissected watersheds on the northern margin of the NFSR watershed.

6. Discussion and Conclusions

The low cost of visNIR spectroscopy recommends it as a method for addressing surface processes in the OCR and elsewhere. In the OCR, the residence time of nearly unweathered material (< 2 k.y.) and old soils (> 350 k.y.) are not well predicted by our weathering function (Fig. 2) because time is required for the weathering signal to manifest and the concentration of weathering products plateaus after a few hundred millennia. These upper and lower limits likely differ between landscapes as a function of lithology, climate, and vegetation.

Our model for soil residence times assumes that the weathering front extends only to the soil-bedrock interface i.e., that bedrock entering the soil column has a constant weathering signature (W_0). This assumption may be violated where erosion rates are slow enough that the hematite weathering front propagates into the bedrock (Mudd and Yoo, 2010). Roadcuts and auger samples in our NFSR site indicate that such deep weathering profiles occur in limited instances.

The residence time distributions for our two watersheds 1) reflect the magnitude of erosional variability due to stochastic hillslope processes and 2) reveal the signature of baselevel controls that can lead to divide migration and catchment reorganization. Our results suggest that soil residence time distributions may enable us to distinguish between steady and transient watersheds and to define the legacy of climate-driven variations in hillslope processes.

7. Bridge

In Chapter II, I used hilltop soils to quantify erosional variability and inferred the processes controlling this variability from the soil residence time distributions. To more

explicitly link process and landscape form, in Chapter III, I designed and executed a series of laboratory experiments wherein I changed the dominant geomorphic process and measured the steady-state topography that resulted.

CHAPTER III

EXPERIMENTAL EVIDENCE FOR HILLSLOPE CONTROL OF LANDSCAPE SCALE

This chapter was published in *Science* in July, 2015. I was the lead author on this study and designed the experimental methodology, conducted the experiments, analyzed the experimental topography, and wrote the manuscript. My co-author Joshua Roering (University of Oregon) acted as the mentor on this project, writing the grant to fund the work, advising on the experimental design, and providing manuscript edits. My other co-author Christopher Ellis performed the technical design and construction of the experimental apparatus, provided technical assistance during experiment runs, and edited the manuscript.

Convex hillslopes and concave valleys are ubiquitous in eroding, soil-mantled landscapes (Davis, 1892; Gilbert, 1909; Moglen et al., 1909; Fig. 4A,B). These distinct landforms are produced by equally distinct sediment transport processes: on hillslopes, abiotic (Matsuoka, 1998; Furbish et al., 2007) and biotic (Gabet, 2000; Roering et al., 2007) disturbance agents disperse sediment downslope, while in valleys, sediment is transported by debris flows (Stock and Dietrich, 2003) or flowing water (Howard, 1994). The transition between hillslopes and valleys has long been considered a fundamental landscape scale (Kirkby, 1971; Montgomery and Dietrich, 1989; Moglen et al., 1998) but there is debate over what controls its style and position. Numerical results suggest that the hillslope-valley transition may be dictated by the minimum runoff necessary for

sediment detachment or landslide initiation (Horton, 1945; Montgomery and Dietrich, 1989; Rinaldo et al., 1995) or by the competition between diffusive transport on hillslopes and advective transport in channels (Smith and Bretherton, 1972; Perron et al., 2009). These geomorphic models predict expansion or contraction of the valley network

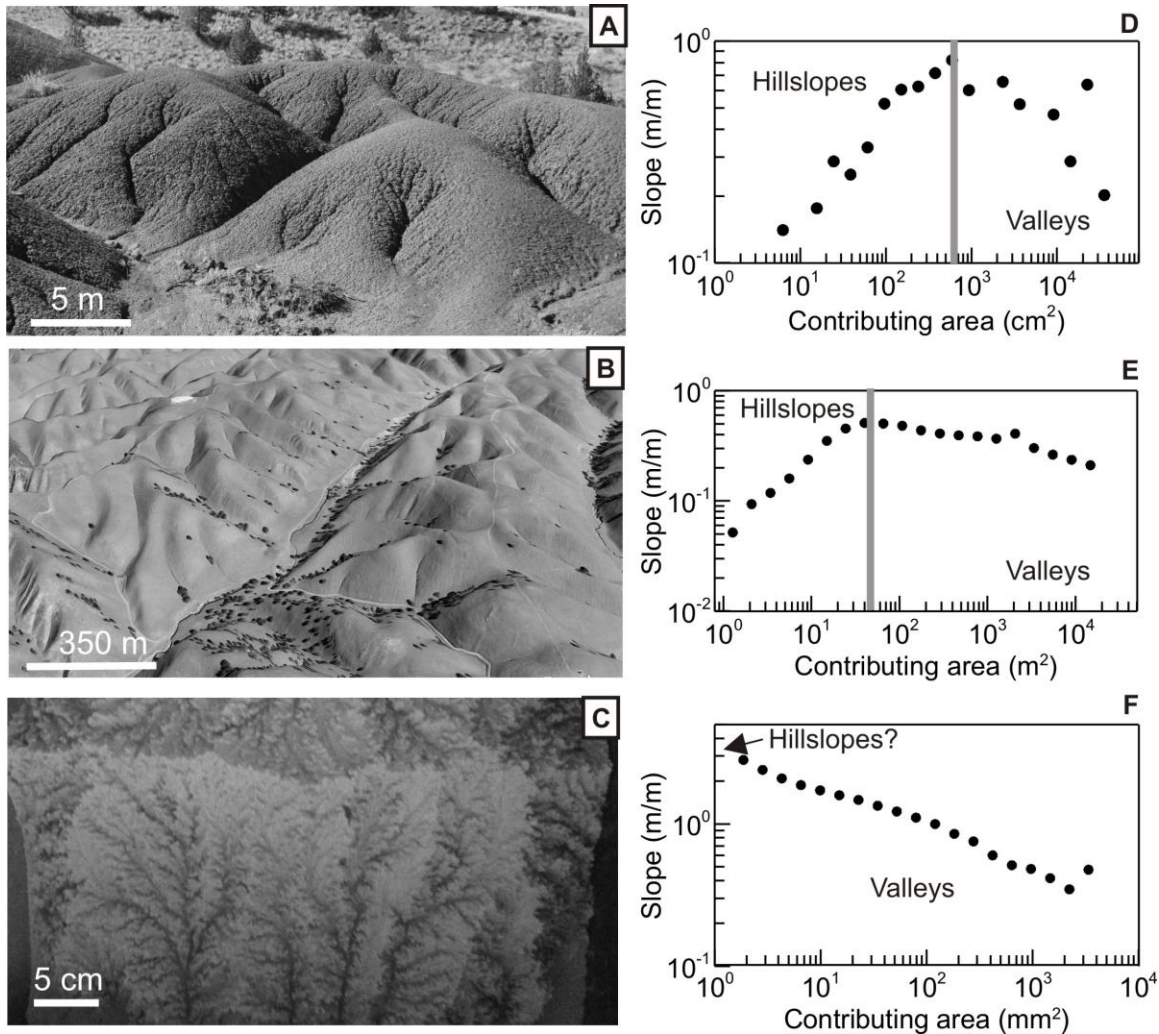


Figure 4. Characteristic morphology of eroding landscapes. Photographs of eroding landscapes: (A): Painted Hills unit of John Day Fossil Beds National Monument, OR, (B): Gabilan Mesa, CA, (C): laboratory landscape from this study with no hillslope diffusion, and associated plots of local slope vs. drainage area, calculated with steepest descent algorithm (D-F). Pictures in (A) and (C) taken by the author, (B) from Google Earth. Topographic data to generate slope-area plots from (D) field surveys, (E) Lidar data from National Center for Airborne Laser Mapping and (F) this study. Grey vertical bars in (D-F) demarcate the inferred hillslope-valley transition (34).

from changes in climatic variables such as precipitation and vegetation (Rinaldo et al., 1995; Tucker and Slingerland, 1997; Moglen et al., 1998). Hence, rigorous testing of controls on the hillslope-valley transition is central to our understanding of landscape response to environmental perturbations. Due to the slow and episodic nature of erosion, however, field tests are limited to comparisons of steady-state model predictions with natural topography (e.g., Gilbert, 1909). Such approaches rely on the assumption that topography reflects long-term average fluxes, ignoring the potentially important effects of initial conditions (Perron and Fagherazzi, 2012) and temporal lags between landscape response and climatic and tectonic forcing (Whipple and Tucker, 1999; Roering et al., 2001).

We conducted a series of laboratory experiments to test whether the competition between hillslope transport and valley incision sets the spatial scale of landscapes (Perron et al., 2009). The theoretical underpinnings of the process control on the hillslope-valley transition derive from a statement of mass conservation, where the rate of elevation change (dz/dt) is equal to uplift rate (U), minus erosion due to disturbance-driven hillslope diffusion and channel advection by surface runoff:

$$\frac{\partial z}{\partial t} = U + D\nabla^2 z - K(PA)^m S^n \quad (1)$$

where D is hillslope diffusivity, K is the stream power constant, A is drainage area, S is slope, P is precipitation rate (assuming steady, uniform rainfall) and m and n are positive constants (Howard, 1994). In this framework, the strength of hillslope transport relative to channel processes can be quantified by the landscape Péclet number (Pe), assuming $n = 1$ (Perron et al., 2009):

$$Pe = \frac{KL^{2m+1}}{D} \quad (2)$$

where L is a horizontal length scale and the hillslope-valley transition occurs at the critical length scale L_c where $Pe = 1$ (Perron et al., 2009). In plots of slope vs. drainage area, L_c corresponds to a local maximum separating convex hillslope and concave valley topography (Perron et al., 2008; Fig 4D,E). If this framework holds for field-scale and experimental landscapes, increasing the vigor of hillslope transport relative to valley incision (decreasing Pe) should result in longer hillslopes (higher L_c) and a contraction of the valley network (i.e., a decrease in drainage density).

Experimental landscapes bridge the gap in complexity between numerical models and natural landscapes (Paola et al., 2009) by enabling us to control the confounding influences of tectonics, climate, and lithology and observe surface evolution through time. As previously noted (e.g., Paola et al., 2009), a complete dynamical scaling of erosional landscapes in the laboratory is typically intractable due to shallow water depths, large grain sizes relative to the size of the experiment, and other considerations. Nonetheless, past landscape experiments have successfully demonstrated the topographic manifestation of changing uplift rate (Lague et al., 2003; Turowski et al., 2006), precipitation rate (Bonne and Crave, 2003), and precipitation patterns (Bonnet, 2009). In these experiments, however, erosion was exclusively driven by surface runoff (e.g., Fig.4C,F), intentionally excluding the representation of diffusive hillslope processes (Lague et al., 2003) and hence precluding tests for the role of hillslope transport in setting landscape scale.

Following Eqn. 1 we created an experimental system that distilled landscape evolution into three essential ingredients: baselevel fall (uplift), surface runoff (channel advection), and sediment disturbance via rainsplash (hillslope diffusion) (Fig. 5). Our experiments in the eXperimental Landscape Model (XLM) at the St. Anthony Falls Laboratory systematically varied the strength of disturbance-driven transport relative to surface runoff (changing Pe) for steady, uniform uplift. The XLM consists of a 0.5 x 0.5 x 0.3 m³ flume with two parallel sliding walls each connected to a voltage-controlled DC motor to simulate relative uplift (Fig. 5A). The experimental substrate was crystalline silica ($D_{50} = 30 \mu\text{m}$) mixed with 33% water to increase cohesion and reduce infiltration (Fig 5C). We began each experiment by filling the XLM with sediment and allowing it to settle for ~24 hours to homogenize moisture content. Topographic data at 0.5 mm vertical accuracy were collected at regular time intervals on a 0.5 mm x 0.5 mm grid using a laser scanner.

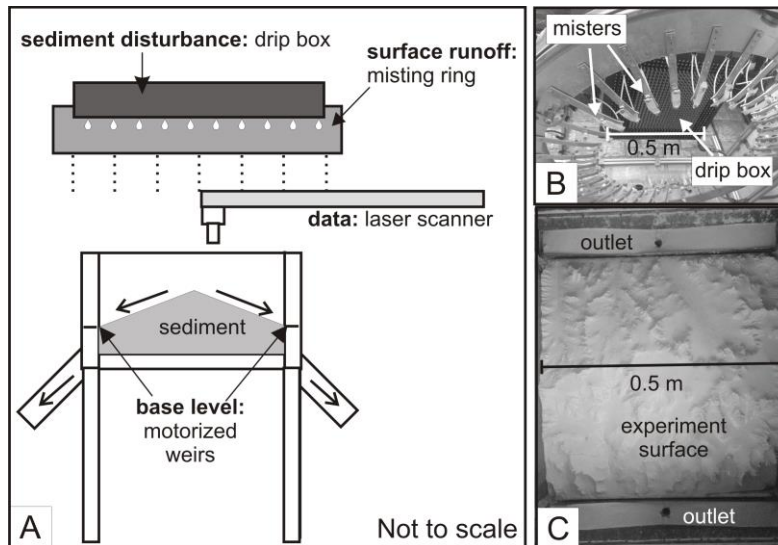


Figure 5. Experimental setup. (A) Schematic profile of experimental apparatus (XLM). Line arrows show direction of sediment movement. (B) Photograph of misting ring and drip box looking from below. (C) Photograph of sediment surface during 100% drip run.

Sediment transport in our experiments was driven by two distinct rainfall systems: the mister, a rotating ring fitted with 42 misting nozzles, and the drip box, a PVC constant head tank fitted with 625 blunt needles of 0.3 mm interior diameter arranged in a 2 cm x 2 cm grid (Fig. 5B). The fine drops produced by the mister lack sufficient energy to disturb sediment on impact and instead result only in surface runoff. By contrast, the 2.8 mm diameter drops from the drip box are sufficiently energetic to create rainsplash and craters on the experiment surface that result in sediment transport. We used four fans mounted on the corners of the experiment to generate turbulence and randomize drop location during drip box rainfall. Importantly, sediment transport due to drip box rainfall consists of both hillslope diffusion from the cumulative effect of drop impacts and non-negligible advective transport due to the subsequent runoff of the drops. Thus, we expect that changing the relative contribution of rainsplash results in a change in both hillslope and channel transport efficiency (D and K , respectively).

We ran five experiments, varying the time of drip box rainfall (i.e., predominantly diffusive transport) from 0 to 100% of total experiment runtime (Fig. 6; Table B1 – see Appendix B for all supplemental figures and tables for this chapter) and holding base level fall and water flux from the mister and the drip box constant. During the experiment, we alternated between drip box rainfall and mister rainfall over 10 minute periods (Table B1); the fans used for drip box rainfall prevented simultaneous operation. We continued each experiment until we reached flux steady-state such that the spatially averaged erosion rate was equal to the rate of base level fall (Figs B1, B2). Each experiment ran for 10 – 15 hours, encompassing 60 – 90 intervals of drip box and/or mister rainfall.

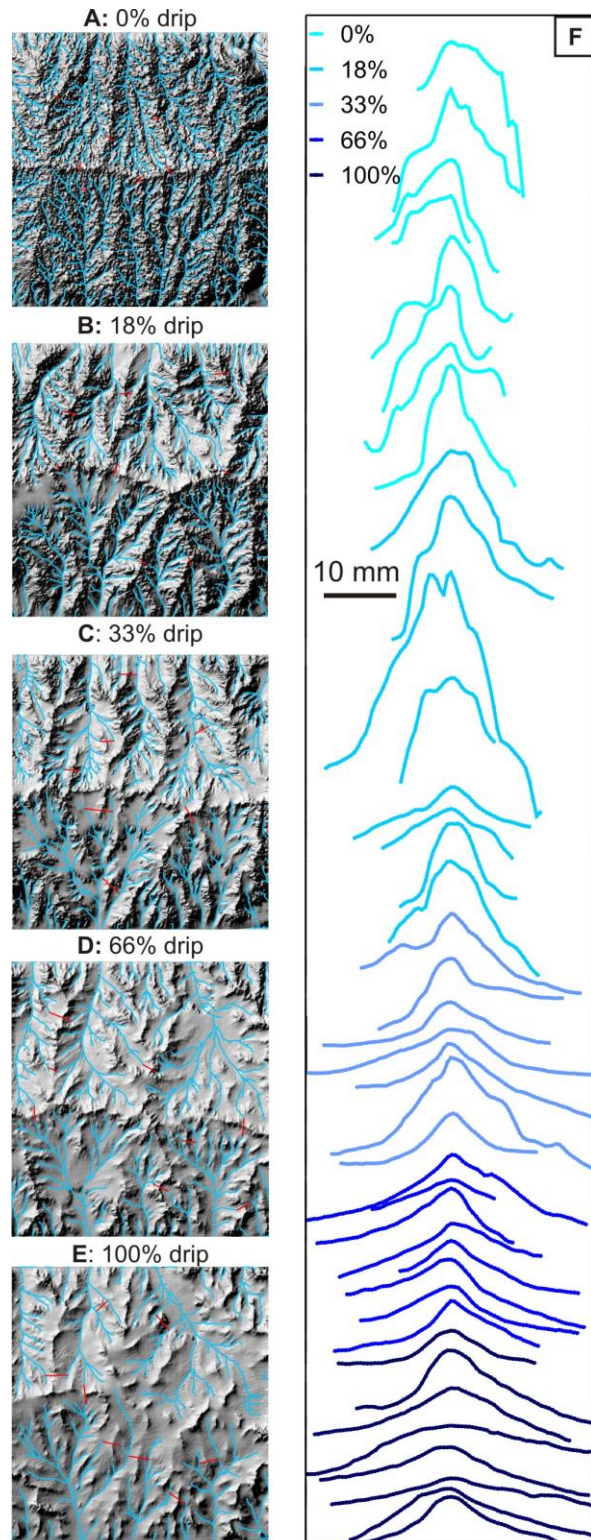


Figure 6. Steady-state topography and hillslope morphology. (A-E) Hillshades of experimental topography for (A) 0% drip (B) 18% drip (C) 33% drip (D) 66% drip and (E) 100% drip overlain with channel networks (blue) and locations of hillslope profiles (red). Topography is 475.5 mm wide in planview. (F) Elevation profiles of hillslopes marked by red lines in (A-E). Vertical and horizontal length scales are equal.

The steady-state topography of our experiments (Fig. 6A-F) demonstrates how increasing the relative dominance of rainsplash disturbance affects landscape morphology. Qualitatively, landscapes formed by a higher percentage of drip box rainfall (Fig. 6E) appear smoother, with wider, more broadly-spaced valleys and extensive unchannelized areas. In contrast, landscapes with more surface runoff transport (Fig 6A), equivalent to past experimental landscapes (Hasbargen and Paola, 2000; Bonnet and Crave, 2003), are densely dissected. As the relative percentage of rainsplash increases, hillslope transects increase in both length and topographic curvature (Fig 6F), confirming that our experimental procedure can be used to adjust hillslope transport efficiency. Hillslope relief in our experiments is approximately 10 – 20% of total landscape relief, a similar value to natural landscapes (Roering et al., 2007).

To test the expected relationship between Péclet number and landscape scale (Perron et al., 2009; Eqn. 2), we used steady-state relationships between landscape morphology and sediment transport laws to independently calculate D and K . This approach is often not possible in natural landscapes and thus extends our theoretical understanding beyond the slope-area plots shown in Figure 4D-F. Specifically, we used the approach of Roering et al. (2007) to calculate D , which uses average hillslope length and gradient, thereby avoiding the stochastic imprint of individual raindrop impacts that can obscure local metrics of hillslope form, such as curvature. The following relationship relates mean hillslope gradient (S) to hillslope length (L_h), critical slope (S_c), erosion rate (E , equal to U at steady state), and hillslope diffusivity (D):

$$\frac{S}{S_c} = \frac{1}{E^*} \left(\sqrt{1 + (E^*)^2} - \ln \left(\frac{1}{2} \left[1 + \sqrt{1 + (E^*)^2} \right] \right) - 1 \right) \quad (3)$$

where $E^* = E(2L_h/DS_c)$ (Roering et al., 2007). To calculate K and m for the stream power model, we used the prediction of Eqn. 1 that steady state channel slope is a power law function of drainage area (Wobus et al., 2006):

$$S = \left(\frac{U}{KP^m} \right)^{\frac{1}{n}} A^{-m/n} \quad (4)$$

To quantify hillslope length and gradient, we mapped the channel network by explicitly identifying channel forms (Wobus et al., 2006; Roering et al., 2008; Passalacqua et al., 2010; Hurst et al., 2012; Fig B3), then traced hillslopes beginning at hilltop pixels by following paths of steepest descent to the nearest channel (Hurst et al., 2012; Fig. B3). We take S_c to be sufficiently large (Table B1) that Eqn. 3 approximates linear diffusion. As the proportion of rainsplash transport increases, D calculated from Eqn. 3 also increases (Table B1), confirming that the morphologic trend of individual hillslope transects (Fig. 6F) reflects increasing hillslope transport efficiency.

To calculate the advective process parameters (Eqn. 4), we extracted slope and steepest descent drainage area data along networks defined by a minimum drainage area of 250 mm^2 (larger than the drainage area of channel initiation) and fit power law relationships to plots of slope vs. drainage area (Wobus et al., 2009). Following Perron et al., (2009) and Lague et al. (2003), we assume that $n = 1$ and use the intercept and slope of the power law fits to calculate m and K for each experiment. While m is relatively invariant for all our experiments, K tends to increase with the fraction of drip box transport, indicating that post-impact rainfall runoff contributes to advective as well as diffusive transport in our experiments.

Given that both D and K change in our experiments, we calculated Pe values (Eqn. 2) for each of our experiments to quantify how diffusive and advective processes contribute to the observed transition from smooth and weakly channelized landscapes (100% drip box; Fig. 6A) to highly dissected terrain (mist only, 0% drip box; Fig. 6E). We calculated the landscape Péclet number, Pe , for each experiment (Eqn. 2), by assuming that $n=1$ and taking the length scale L to be the horizontal distance from the main divide to the outlet (256 mm). Our results show that landscape Pe value increases with the fraction of drip box transport, demonstrating that an increase in hillslope transport efficiency, D , is the dominant result of increasing rainsplash frequency. Figure 7 reveals a positive relationship between Pe and drainage density, which is inversely related to hillslope length or L_c , such that increasing Pe in our experiments results in higher drainage density (i.e., shorter hillslopes).

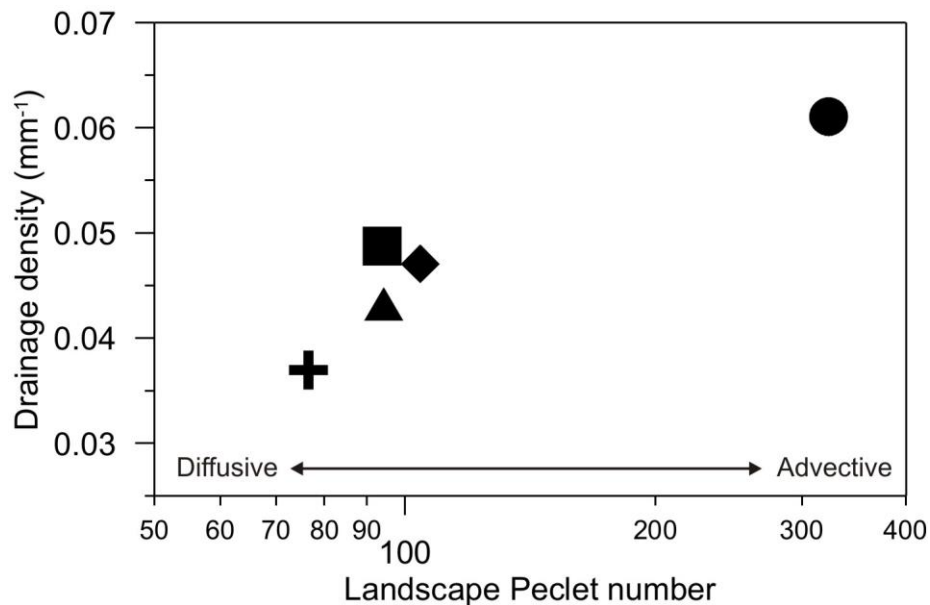


Figure 7. Effect of landscape Péclet number on landscape scale. Landscape Peclet number for each experiment (circle, 0% drip; square, 18% drip; diamond, 33% drip; triangle, 66% drip; plus sign, 100% drip) vs. drainage density of GeoNet-derived drainage networks.

This finding is consistent with theoretical predictions for coupled hillslope-channel process controls on the scale of landscape dissection (Smith and Bretherton, 1972; Perron et al., 2009).

In our experiments, hillslope transport imparts a first-order control on landscape scale, emphasizing the need to establish functional relationships between climate variables and hillslope process rates and mechanisms for real landscapes. While climate change scenarios typically focus on the influence of vegetation and rainfall on overland flow and channel hydraulics (Rinaldo et al., 1995; Moglen et al., 1998), climate controls on the vigor of hillslope transport (e.g., Dixon et al., 2009; Chadwick et al., 2013) can drive changes in landscape form. Robust linkages between transport processes and topography, as discussed here, are an important component of interpreting planetary surfaces as well as decoding paleo-landscapes and sedimentary deposits.

1. Bridge

In chapter III I used analog experiments to show how the efficiency of hillslope transport relative to channel incision sets the scale of eroding landscapes. In Chapter IV, I present a field investigation of the early stages of erosive landscape evolution on a basaltic lava flow in the High Cascades. I use a mechanistic model of fluvial incision to demonstrate that while extreme events such as outburst floods may be responsible for initiating channel formation, smaller annual channel discharges are also geomorphically important.

CHAPTER IV

RAPID FLUVIAL INCISION OF A LATE HOLOCENE LAVA FLOW: INSIGHTS FROM LIDAR, ALLUVIAL STRATIGRAPHY, AND NUMERICAL MODELING

This chapter is in preparation for submission to the *Geological Society of America Bulletin*. I was the lead author on this study, and performed the topographic and stratigraphic analyses, designed the modeling approach, and ran the numerical model. My co-author Joshua Roering served as a mentor on this project, introducing me to the site, assisting in field work and analysis, and editing previous versions of the manuscript.

1. What Sets the Pace of Fluvial Incision in Volcanic Landscapes?

Effusive volcanic eruptions reset fluvial landscapes by paving over channel networks, killing and damaging vegetation, and burying soils (Jefferson et al., 2014). Though volcanic landscape disturbance has been well documented in modern explosive eruptions (Major et al., 2000; Gran and Montgomery, 2005; Swanson et al., 2013), the processes driving the post-eruption fluvial dissection of lava flows are relatively unconstrained (Jefferson et al., 2010; Deligne et al., 2013). Blocky lava flows, whose high surface permeability (Freeze and Cherry, 1979) and low nutrient content (Deligne et al., 2013) inhibit both surface water and vegetation growth (Jefferson et al., 2014), present a particular conundrum in volcanic landscape evolution. Previous workers have proposed that permeability reduction via in-situ weathering (e.g., Lohse and Dietrich,

2005), is essential for enabling drainage development in these systems (Jefferson et al., 2010).

There are many prominent canyons incised into lava flows where soil development is limited or absent (Lamb et al., 2008a; Lamb et al., 2014; Baynes et al., 2015). Investigation of these channels has demonstrated that they formed as a result of catastrophic floods known as “megafloods”, which are in excess of the magnitude of meteorologic events (O’Connor and Costa, 2008). The channels are cut into columnar basalt flows, where prominent sets of vertical joints enable rapid incision via plucking (Whipple et al., 2000a) or block toppling (Lamb and Dietrich, 2009). For these systems, smaller discharges cannot mobilize the blocks produced during the megafloods or perhaps lack tools to perform abrasion (e.g., Baynes et al., 2015), and are hence unable to incise the bed

Columnar jointing is not a ubiquitous feature of all lava flows. Blocky lava flows, associated with stratovolcanoes and volcanic fields worldwide, are comprised of a rubbly surface layer and a coherent, massive core (Kilburn, 2000). In the absence of jointing, it is not apparent that the rapid plucking by megafloods (Lamb et al., 2008a; Lamb et al., 2014; Baynes et al., 2015) drives incision in these landscapes. Nevertheless, in landscapes where blocky lava flows and alpine glaciation or very large landslides co-occur, it is likely that lava flows are subject to large discharge events in the form of dam breach floods (O’Connor and Costa, 2008). These events have the potential to provide the tools and geomorphic power necessary to form fluvial channels. Hence, determining the rate and style of fluvial processes in these systems is essential to understanding the evolution of temperate volcanic landscapes.

2. Approach and Scope

Here, we focus on Collier lava flow, a basaltic andesite flow in the High Cascades of Oregon (Fig. 8) that has been incised up to 8 m by White Branch Creek (Fig. 9). Using a combination of field evidence, high-resolution lidar topography, and numerical modeling, we ask: Can megafloods achieve rapid incision through abrasion rather than plucking? If the channel bed is not mantled by large joint blocks, can smaller discharges be relevant for channel incision (e.g., Wolman and Miller, 1960)?

To predict incision rates along White Branch Creek, we use a 1D mechanistic model of bedrock abrasion by total sediment load (Lamb et al., 2008b). Sediment supply has a strong influence on the fluvial incision of bedrock, both enhancing incision by acting as tools for abrasion and impeding incision by protecting the bed from grain impacts (Gilbert, 1877). Despite a recent proliferation of theoretical models translating this concept into mathematical formulations (Sklar and Dietrich, 2004; Turowski et al., 2007; Lamb et al., 2008b; Chatanantavet and Parker, 2009) field application has been mostly limited to inferring the relative dominance of tools and cover for specific fluvial systems (Turowski and Rickenmann, 2009; Cook et al., 2013; Scheingross et al., 2014). Prediction of fluvial incision rates or model tests at the reach scale has been rare (excepting Hobbie et al., (2011)) owing to the difficulty in measuring high-resolution incision rates and key model parameters (e.g., sediment supply) in natural landscapes.

The undissected surface of Collier lava flow enables us to confidently calculate pre-incision topography and hence incision rate along the channel (Ferrier et al., 2013), making this site uniquely suited to using mechanistic models of bedrock abrasion to

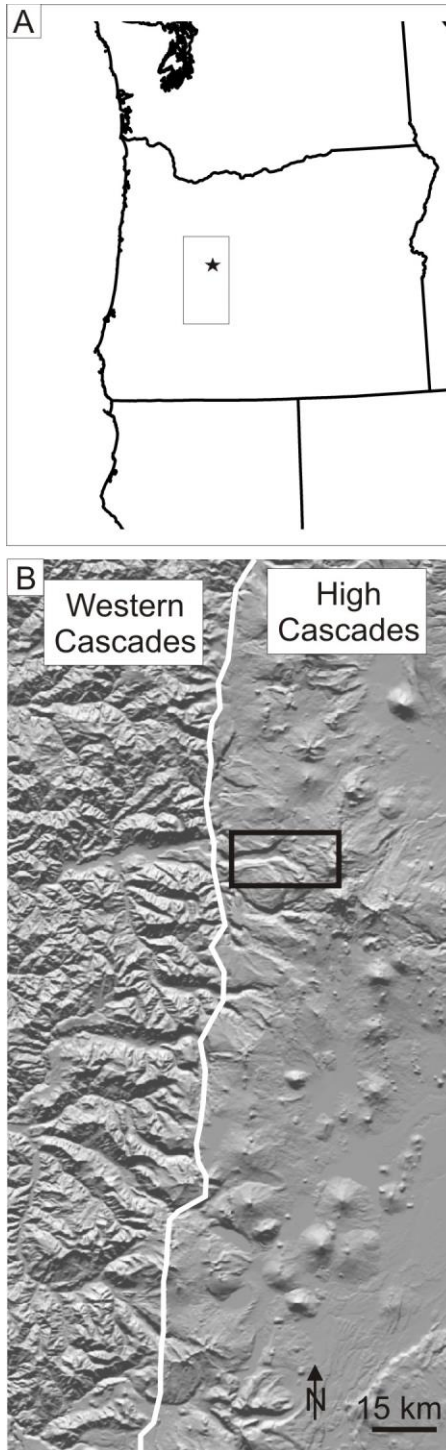


Figure 8. Regional setting. A. Study location marked by black star in state outline of Oregon. Gray box delineates area of B. Hillshade of the Central Oregon Cascades. White line marks boundary between dissected Western Cascades and undissected High Cascades. Black box shows location of Figure 9.

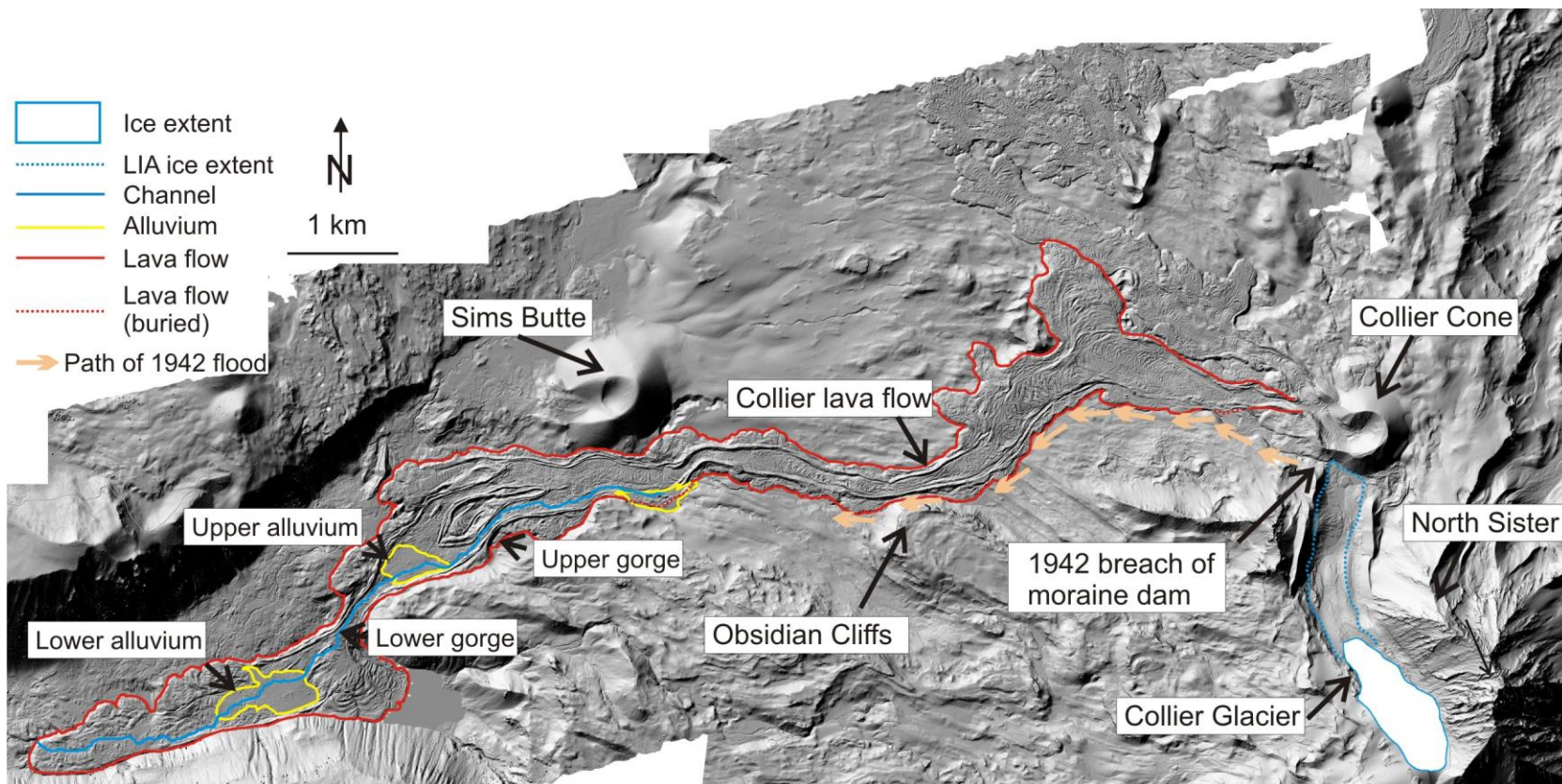


Figure 9. Geologic setting of Collier lava flow A. Lidar hillshade of study area, showing Collier lava flow (red outline), Collier glacier (white polygon with blue outline) and White Branch Creek (solid blue line). Dotted blue line shows LIA ice extent of Collier Glacier, orange arrows show path of 1942 outburst flood (O'Connor, et al., 2001), yellow outlines alluvial deposits. A and A' show extent of long profile shown in Figure 10. Channel flow is from east-northeast to west-southwest.

model channel-forming discharges. Furthermore, the mixed bedrock-alluvial nature of the channel (Figs. 9-11) enables us to place constraints on long-term sediment supply, which is often impossible for bedrock channels. Our model results demonstrate that outburst floods alone cannot account for the incision we observe, implying that smaller events

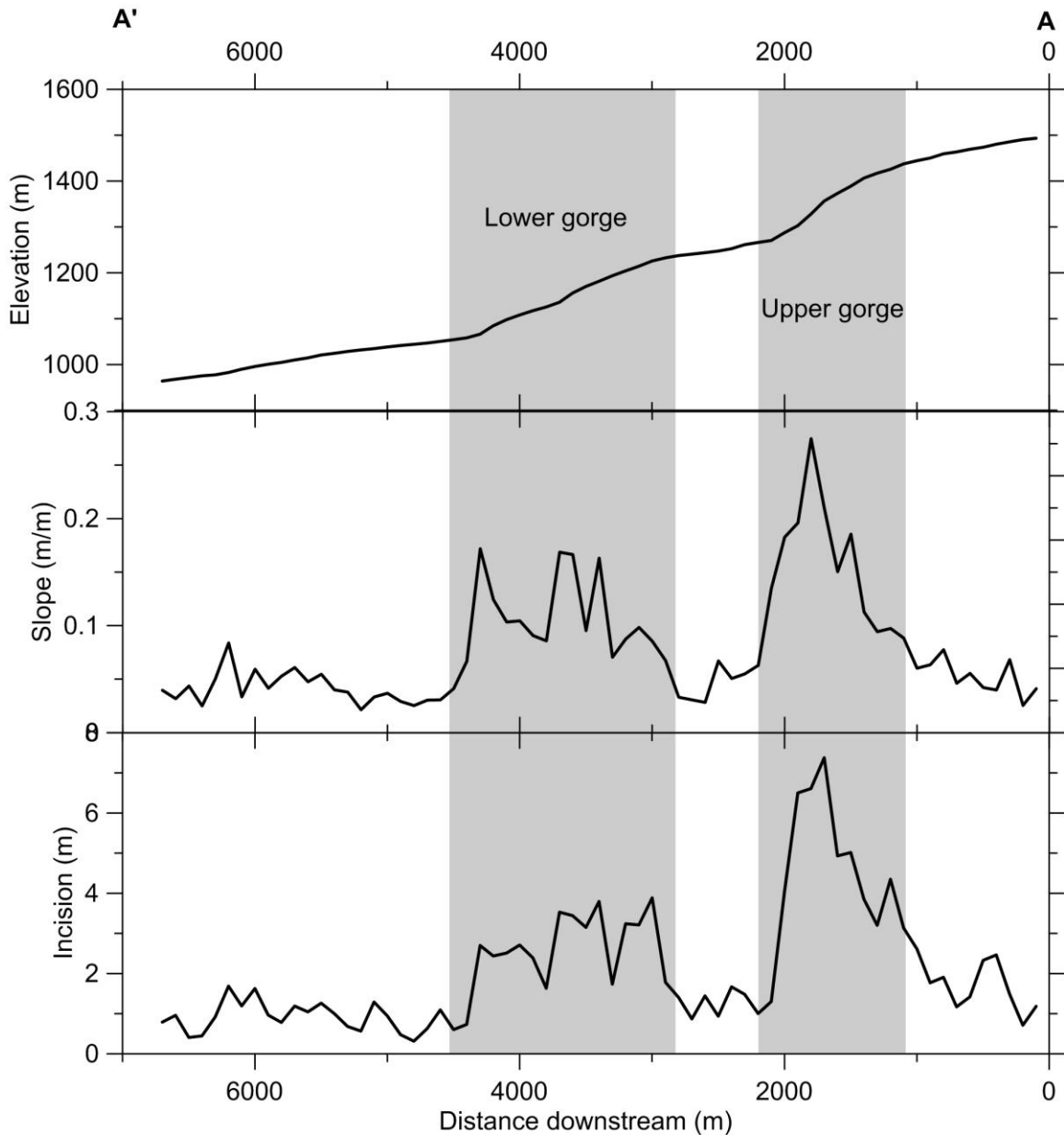


Figure 10. Channel morphology and topography A. Long profile, B. Slope, C. Incision measured by differencing thalweg and interpolated pre-incision surface (see text for details). Raw data is smoothed to 100 m spacing (~10 channel widths). Grey boxes indicate extent of bedrock gorges. Note correspondence of maxima in slope and incision.

play an important role in the evolution of this channel.

3. Volcanic and Glacial Setting

The Cascade Range, which extends from northern California to southern British Columbia, is a volcanic arc associated with the subduction of the Juan de Fuca Plate under the North American Plate. In Oregon the Cascades are divided into two physiographic provinces: the largely inactive, steep and highly dissected Western Cascades, and the High Cascades, where numerous cinder cones, stratovolcanoes, and other vents have been active throughout the Holocene (Fig. 8; Jefferson et al., 2010). The border between these provinces is clear in both topography (Fig. 8) and hydrology, with most precipitation in the High Cascades running off as groundwater and emerging in a linear trend of springs along the High Cascades/Western Cascades boundary (Jefferson et al., 2010).

Most Cascade stratovolcanoes have been dissected by alpine glaciers. Moraine mapping points to multiple post-LGM glacial highstands in the Oregon Cascades (Marcott et al., 2009), with the most recent occurring during the Little Ice Age (LIA), ~ 150 - 300 years ago. Cascade glaciers have retreated substantially since the LIA, leading to several documented moraine-dam breaches in the past century (Hopson, 1960; O'Connor et al., 2001).

Collier lava flow erupted from Collier Cone, a cinder cone on the western flank of North Sister in the High Cascades of Oregon that formed ~1600 years ago (Fig. 9; Sherrod et al., 2004). The morphology of the lava flow reflects the thermal and topographic conditions of emplacement (Deardorff and Cashman, 2012). The top meter

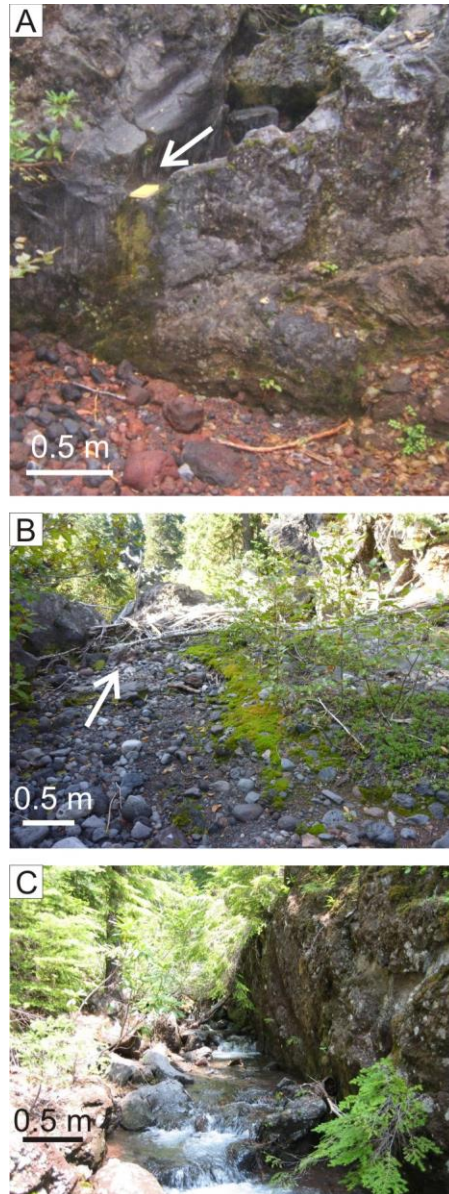


Figure 11. Field expression of channel morphology. A. Abraded knickpoint lip in lower bedrock gorge, B. Alluvial reach, C. Snowmelt discharge observed in 2008 (photo: J. Roering). White arrows in A and B indicate flow direction. Flow in C is directed out of the page.

of the flow, which cooled quickly, is highly brecciated with individual blocks up to ~ 1 m in diameter, while the slow-cooled core is massive and coherent. Lava flow width is broadly correlated with slope, i.e., steep sections are narrow and flat sections are wide (Deardorff and Cashman, 2012).

Collier Glacier is located upstream of Collier lava flow between the stratovolcanoes North and Middle Sister (Fig. 9). The lateral LIA moraines of Collier Glacier run perpendicular to Collier Cone; the LIA terminus of Collier Glacier intersected Collier Cone and has caused localized slope failure on the cone's flank (Fig. 9). During 20th century glacial retreat, a moraine-dammed lake formed, draining catastrophically in 1942 (Hopson, 1960) and producing a large sediment-laden flood with discharge as high as 500 m³/s (O'Connor et al., 2001) that deposited sediment up to ~8 km downstream of the moraine dam breach (Fig. 9). The breach is still visible as a ~ 5 m deep incised notch between Collier Cone and the lateral moraine (Fig. 9). The lake drained partially again sometime between 1954 and 1956, creating a new incisional notch to the north of the 1942 outburst, but did not have major downstream impacts (Hopson, 1960; O'Connor et al., 2001).

4. Methods

4.1. Measuring Channel Morphology and Incision

We used elevations from high-resolution airborne lidar (Deardorff and Cashman, 2012; NCALM, 2008) to map the morphology of White Branch Creek where it runs over Collier lava flow (Fig. 9,10). Because the channel lacks clear bankfull indicators (Fig. 11), we mapped the banks and thalweg of the gorge manually from ArcGIS hillshades and channel cross-sections, labeling the lowest point in each cross-section as the thalweg and marking prominent points of inflection on either side of the thalweg as banks. To calculate incision in the gorges (Fig. 9), we mapped the location of the uneroded Collier lava flow surface along the length of White Branch Creek and used these elevations to interpolate a pre-incision surface (Ferrier et al., 2013). Local incision along the channel

(Fig. 10) is then defined as the elevation of the pre-incision surface minus the elevation of the modern thalweg.

4.2. Alluvial Stratigraphy and Radiocarbon Sampling

To constrain the timing of channel-forming discharge events and discriminate between fluvial and debris flow processes, we dug 6 soil pits in the alluvial deposits on Collier lava flow, 3 on the upper deposit and 3 on the lower deposit (Fig. 12), supplementing existing work by Deligne et al. (2013). We excavated each pit until we reached the lava flow surface or until the depth of the pit precluded continuing safely. We documented and measured the deposits (Fig. 13; Table C1 – see Appendix C for all supplemental tables and figures for this chapter) and, where possible, collected charcoal for radiocarbon dating. Radiocarbon samples were processed and analyzed at the University

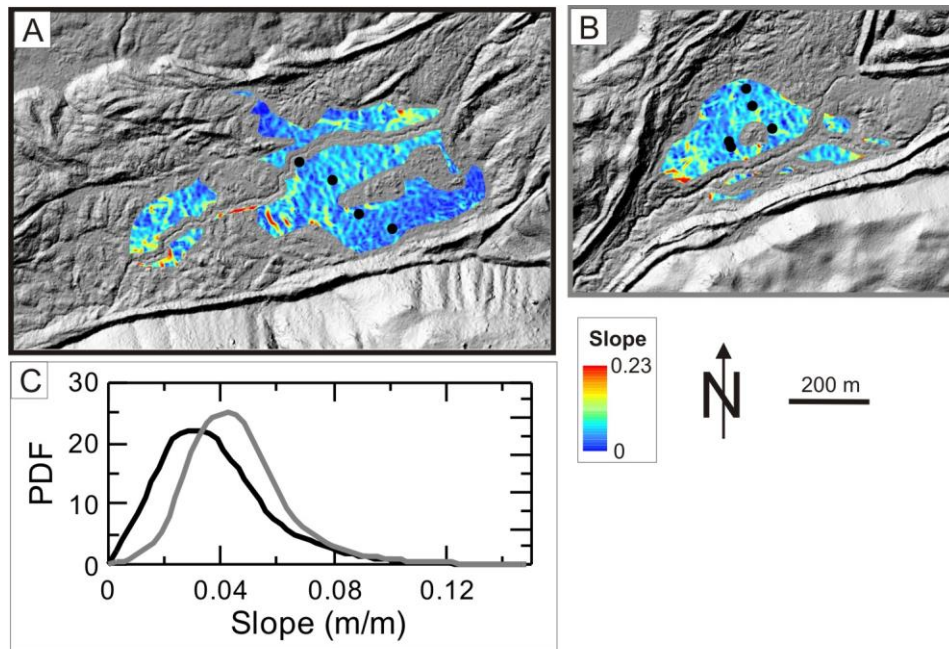


Figure 12. Slope of alluvium. Lidar-derived slope maps for A. Lower alluvium and B. Upper alluvium. C. Probability density function of slope maps shown in A (black) and B (grey). Both alluvial surfaces have a mean gradient of ~ 0.04 . Pit locations are shown by black circles

of Arizona AMS lab following standard techniques. We used these data and stratigraphic relationships where available to build an age model for the deposits using OxCal v.4.1.7 (Fig. 14; Bronk Ramsey, 2009).

5. Field Evidence for Incision Mechanisms and Timing

Since lava flow emplacement, White Branch Creek has incised two bedrock gorges up to 8 m deep into the flow and deposited $> 0.2 \text{ km}^3$ of sediment in two alluvial plains (Deligne et al., 2013; Figs. 9-11). The boundaries between these reaches correspond with major breaks in the background slope and width of Collier lava flow (Fig. 9): bedrock gorges occur where the flow is steep and narrow, while alluvial deposits are located in relatively flat areas. The bedrock gorges are significantly steeper (average gradient of 0.11) than the alluvial reaches (average slope of 0.04), mimicking the pattern of the background topography.

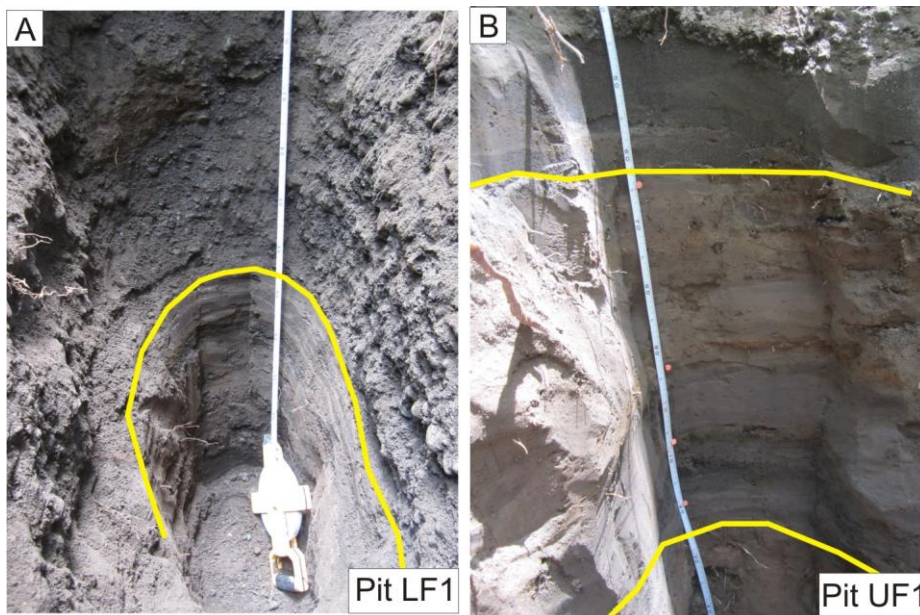


Figure 13. Pit stratigraphy. Field photos of A. Pit LF1 and B. Pit UF1. Yellow lines mark boundaries of normally graded packets deposited by discrete clear water flows.

5.1. Gorge Morphology: Pre-incision Topography and Sediment Provenance

The channel walls and bed of the bedrock reaches are smooth and often fluted or potholed (Fig. 11A), consistent with abrasion by sediment impacts (Whipple et al., 2000a; Sklar and Dietrich, 2004). At the 100 m scale (~10 channel widths) slope is strongly correlated with gorge depth (Fig. 15A), indicating that shear stress is the primary control on channel incision rather than variations in rock hardness or other factors (Sklar and Dietrich, 2001). Channel slope is also correlated with the slope of the pre-incision lava flow surface (Fig 15B). This pre-incision topographic control may explain why observed channel slopes are well in excess of typical fluvial values (~0.05; Montgomery, 2001), despite the lack of debris flow activity.

Though the bed is generally bare, patches of alluvium occur locally within the bedrock gorges. These alluvial patches contain clasts of Collier lava flow as well as abraded clasts of obsidian (Fig. 11B). The presence of obsidian strongly suggests that despite the absence of paleohydraulic indicators like those found upstream of the lava flow (O'Connor et al., 2001), the discharge events responsible for carving the channel traversed the channel adjacent to the Obsidian Cliffs (Fig 9), possibly en route from Collier Glacier.

5.2. Alluvial Morphology: Implications for Sediment Transport

White Branch Creek has formed three significant alluvial deposits on Collier lava flow (Deligne et al., 2013). We focus on the two that are downstream of the bedrock reaches, as they enable us to draw conclusions about the flux and caliber of sediment moving through the incisional reaches. The thick forest vegetation on these alluvial

deposits is in stark contrast to the unaltered surface of Collier lava flow, which remains largely unvegetated (Deardorff and Cashman, 2012; Deligne et al., 2013). In these alluvial reaches, the channel of White Branch Creek is formed in the sediment of the deposits (e.g., Parker, 1978), i.e., there is no bedrock exposed in the bed. In addition to the main channel, there are several inactive channels on the alluvial deposits filled with organic debris, suggesting that the channel location in these reaches has not been fixed through time. When the active channel and exposed lava flow are excluded, the alluvial surfaces have a consistent slope of ~ 0.04 (Fig. 12C).

Mackin (1948) posited that over time channel slope adjusts to provide sufficient power to both transport the sediment supplied to the channel and to incise the channel bed at a rate matching uplift rate. In incising bedrock channels, this suggests that the ability of the channel to transport sediment (known as sediment transport capacity) is in excess of long-term sediment supply (e.g. Sklar and Dietrich, 2006; Johnson et al., 2009), while in alluvial systems, such as the alluvial reaches of White Branch Creek, transport capacity is equal to or less than supply. Long-term transport conditions have also been demonstrated to control the surface slope of alluvial fans (Stock et al., 2008 and references therein). Given that the alluvial reaches of White Branch Creek are not incising, we can use the surface slope and channel geometry to calculate sediment transport capacity (see details under Model Formulation and Procedure), thereby setting a lower bound on the long-term rate of sediment supply in the bedrock gorges.

5.3. Alluvial Stratigraphy

Sediment in the six alluvial soil pits (locations shown in Figure 12) ranges from silt to large cobbles (Table C1). Each pit contains decimeter-scale normally-graded

packets (Fig. 13) with abrupt basal boundaries; buried organic material is present in the pits, but soil horizonation is absent (Table C1; cf. Deligne et al., 2013). Though our data are too sparse to correlate stratigraphy, our observations are consistent with emplacement by clear water fluvial processes (Collinson et al., 2006), confirming the findings of past work on Collier lava flow (Deligne et al., 2013). Radiocarbon analyses of charcoal from two pits on the upper deposit (UF1 and UF2) and one on the lower deposit (LF2) yielded 95% confidence intervals of 580 – 397 cal y.b.p., 1345 – 1141 cal y.b.p., and 537 – 412 cal y.b.p., respectively (Fig. 14). These dates suggest that incision and associated deposition began shortly after lava flow emplacement 1600 years ago and has continued since, pointing to the role of multiple events rather than a single catastrophic channel-forming flood (e.g., Lamb and Fonstad, 2010).

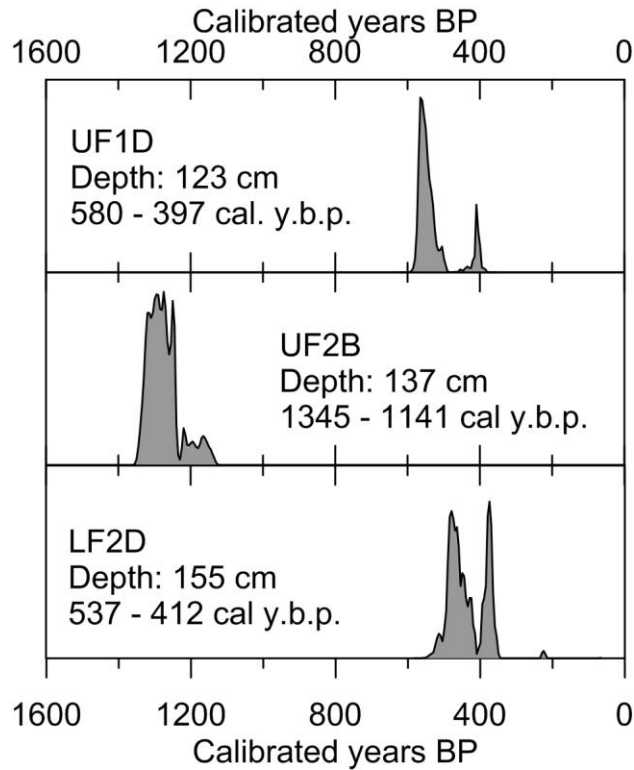


Figure 14. Radiocarbon dating of alluvial deposits. Age probability density functions for three radiocarbon samples: UF1D, UF2B, and LF2D.

5.4. Hydrologic Regime

Field observations indicate two sources of discharge in White Branch Creek: snowmelt runoff and glacial outburst floods from moraine dam breaches at Collier Glacier. During June 2008, we observed shallow discharge in both the bedrock gorges and alluvial reaches, which given that the snowpack of 2007-08 was not exceptional (based on SNOTEL data), we infer occurs on an approximately annual basis. As noted above, there is also historical record of moraine-dam breaches at Collier Glacier (Hopson, 1960). Though it does not appear that these recorded events reached the uppermost alluvial deposit (O'Connor et al., 2001), the presence of obsidian clasts and other externally sourced sediment on the lava flow leads us to conclude that similar events may have traveled farther downstream (i.e., onto the lava flow) in the past.

6. Modeling Philosophy: Assessing the Driving Forces of Incision

Field observations, lidar topography, and alluvial stratigraphy enable us to draw reasonable inferences about the incision of Collier lava flow and the concomitant onset of post-eruption landscape evolution. However, it is not clear from the evidence described in the previous section how the two discharge regimes conspire to provide geomorphic power to the channel. Could the channel have been carved solely by glacial outburst floods? Or does annual snowmelt discharge play a role? To answer these questions, we set out to model the incision of Collier lava flow numerically, using the channel morphology measured from lidar as model input and constraining other model parameters with our field observations.

In selecting a model, we begin by considering the simplest formulation that shed light on the discharge events driving the formation of White Branch Creek. The close

correlation between channel slope and local incision (Fig. 15) suggests that the stream power law of bedrock erosion (Howard, 1994) may be appropriate for this system, where erosion rate E is a function of channel slope S , drainage area A and positive constants K , m , and n :

$$E = KA^m S^n \quad (1)$$

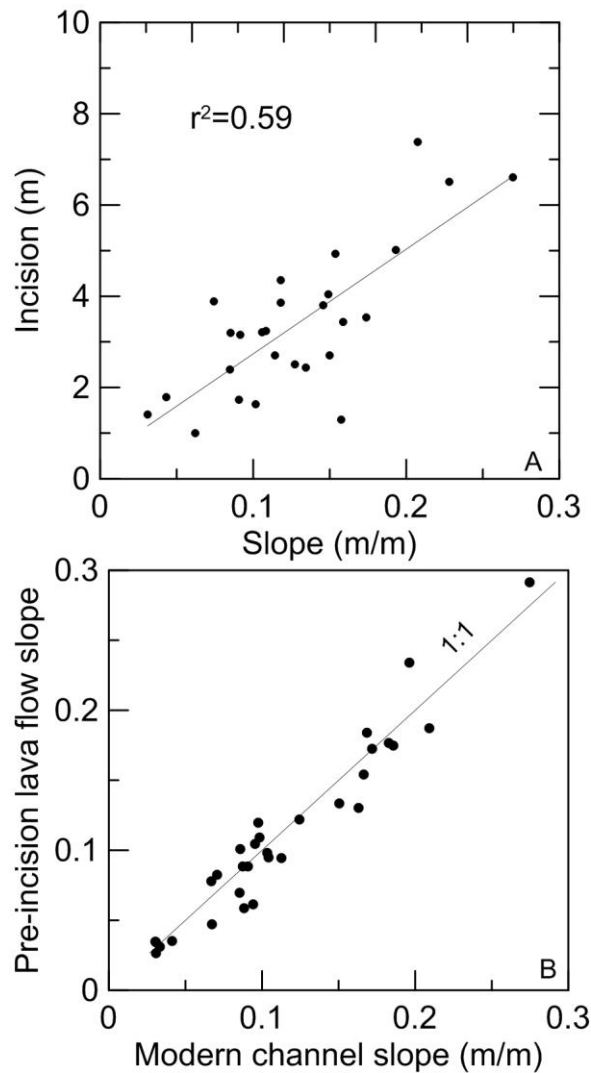


Figure 15. Correlation between slope and incision. A. Channel slope (smoothed to 100 m spacing) is positively correlated with total amount of incision in bedrock gorges. B. Channel slope is also correlated with the slope of the pre-incision surface.

The stream power model has considerable utility in tectonic geomorphology, where steady-state channel morphology can be taken as a proxy for uplift rate (Wobus et al., 2006), or in comparisons of channels incising into different material (Sklar and Dietrich, 2001) or under different climate conditions (Ferrier et al., 2013). However, fitting the stream power model to the incision patterns we observe in White Branch Creek leaves us no wiser than Figure 15: slope controls incision, but the fit values of K , m , and n do not increase our understanding of the system, given similar climate, tectonics, and rock strength along the length of this relatively short channel. In particular, these parameters do not have bearing on the erosive capacity of the discharge events that we have suggested occur in this channel.

Given the limitations of the stream power model, we instead use a formulation that describes the physical process of fluvial erosion of bedrock via sediment abrasion (Lamb et al., 2008b). Bedrock incision occurs via two primary processes: plucking, whereby jointed blocks are removed from the bed by flowing water (Whipple et al., 2000a; Chatanantavet and Parker, 2009; Lamb and Dietrich, 2009), and abrasion, whereby sediment grains impacting the bed gradually erode it via mechanical wear (e.g., Sklar and Dietrich, 2004). Plucking tends to dominate in highly fractured bedrock and produces large blocks, while abrasion dominates in massive, intact bedrock and forms potholes, flutes, and other sculpted features (Whipple et al., 2000).

There is abundant evidence for fluvial abrasion in the gorges of White Branch Creek (i.e., potholes, smooth walls, flutes; Fig 11A; Wohl and Merritt, 2001), and we observe limited large blocks or cavities that might indicate a plucking-dominated channel (e.g., Whipple et al., 2000b; Lamb and Fonstad, 2010). The channel bed is primarily cut

into the solid inner core of the lava flow, rather than the rubbly surface layer, which was presumably removed early in the incision process (e.g., Whipple et al., 2000b).

7. Model Formulation and Procedure

7.1. Assumptions and Parameter Constraints

All sediment-dependent models of bedrock incision (Sklar and Dietrich, 2004; Turowski et al., 2007; Lamb et al., 2008b; Chatanantavet and Parker, 2009) require sediment supply, grain size, and bed shear stress as input values. Our field observations allow us to put bounds on the range of these quantities, but we lack sufficient information to constrain the most likely parameter combinations or to define the shape of the parameter distributions. In acknowledgment of this uncertainty, we use a Monte Carlo algorithm in which we select a different set of these three parameters (grain size, sediment supply, and channel discharge) for each model run from a uniform distribution of possible values, the bounds of which are set as described below.

7.1.1. Discharge and Shear Stress: A primary goal of this work is to model discharges ranging from annual snowmelt flows to large outburst floods. We set the lower bound of the discharge range based on the previously described observation of ~0.5 m deep snowmelt discharge in June 2008, which we estimate corresponds to a discharge of ~1 m³/s. Past work on historical outburst floods from Collier Glacier reports peak discharges at the downstream extent of the flood as 40 m³/s (O'Connor et al., 2001). We set the upper bound of our discharge range at 120 m³/s to incorporate the possibility that prehistoric floods exceeded the magnitude of those observed historically.

Converting discharge to bed shear stress requires quantifying flow hydraulics. The hydraulics of steep mountain channels are sufficiently complex that there is no

accepted formulation for bed shear stress in these environments (cf. Wohl, 2000). Instead, we follow previous authors (e.g., Sklar and Dietrich, 2004) in using the depth-slope product to calculate bed shear stress for White Branch Creek:

$$\tau_b = \rho_w g H S \quad (2)$$

where ρ_w is the density of water, g is the acceleration of gravity, and H is channel depth. We calculate depth, H , by iteratively solving the 1D energy equation (HECRAS, 2008), since White Branch Creek is ungauged and neither of the historical outburst floods from Collier Glacier were observed in our study reaches. Due to the high channel slopes of White Branch Creek (see discussion above in Field Evidence section), the energy equation predicts supercritical flow conditions for the length of the channel. Prolonged supercritical flow is unreasonable in hydraulically rough channels like White Branch Creek, which tend to have high rates of energy dissipation (Montgomery and Buffington, 1997). Hence, when the energy equation predicts supercritical flow in the channel, our model defaults to the critical depth, such that H is a function of channel width w and instantaneous discharge Q :

$$H = (Q/w)^{2/3} g^{-1/3} \quad (3)$$

7.1.2. Grain Size: Sediment in the modern bedrock channel and on the alluvial plains ranges in size from silt to coarse cobbles. Due to this breadth of grain sizes, we err on the side of inclusion for our model inputs, selecting grain size diameters between 0.001 to 0.5 m.

7.1.3. *Sediment Supply*: As discussed above, in fluvial settings dominated by deposition or transport, landforms are created by the balance between sediment transport capacity and sediment supply (Stock et al., 2008; Johnson et al., 2009). With this in mind, we use the surface slope of the alluvial deposits and the average geometry of the modern channel to calculate bedload transport capacity q_t in the alluvial reaches. For consistency with the literature (Sklar and Dietrich, 2004; Lamb et al., 2008b; Scheingross et al., 2014), we use the Fernandez-Luque and van Beek (1976) relation for bedload transport capacity, which states that sediment transport capacity is a power-law function of bed shear stress:

$$q_{bc} = 5.7(RgD^3)^{1/2}(\tau_* - \tau_{*c})^{3/2} \quad (4)$$

where R is the specific density of sediment, D is the average diameter of sediment grains, and dimensionless bed shear stress τ_* is defined as $\frac{\tau_b}{(\rho_s - \rho_w)gD}$. For each model run, we use the selected values of discharge and grain size, and the average width of the modern alluvial channel to calculate bed shear stress in the alluvial reaches (equation 2). The bedload transport capacity calculated by equation 3 is then the lower bound of the sediment supply parameter space. In using modern channel geometry to calculate bedload transport capacity, we assume that channel shape reflects long-term flow conditions (e.g., Parker, 1978).

7.2. *Mechanistic Modeling of Bedrock Abrasion*

Mechanistic models of fluvial abrasion by sediment impacts state that erosion rate E is a product of the average volume of sediment removed per impact, V , the impact rate

per unit bed area, I , and the fraction of the bed that is exposed to abrasion, F (Sklar and Dietrich, 2004; Turowski et al., 2007; Lamb et al., 2008b):

$$E = V I \quad (5)$$

The first version of these models (Sklar and Dietrich, 2004) considers only impacts from sediment traveling as saltating bedload and uses the hop length and kinetic energy of sediment grains to calculate I and V . As transport stage increases towards the threshold of suspension ($\tau^* \approx 20$), the hop lengths become infinitely long, making I (and, by extension, E) go to zero. Lamb et al. (2008b) recast this model in terms of total load, recognizing that due to turbulent fluctuations, even sediment that mostly travels in suspension comes in contact with the bed and is hence important to fluvial abrasion.

For most bedrock systems, the contribution of suspended load to erosion is relatively small compared to bedload, but for rivers with large discharges and/or small grain size, the difference between bedload-only models and the total load model is non-negligible (Scheingross et al., 2014). Due to high discharge of outburst floods (O'Connor et al., 2001) and the relatively small grain sizes we observe, we used the total load formulation (Lamb et al., 2008b) to model instantaneous incision rates in White Branch Creek.

7.3. Governing Equations

To calculate E with the total load model, we use equation 36 of Lamb et al. (2008b), which states that E is a function of material parameters, sediment flux, the partition of sediment between suspension and bedload, and channel flow:

$$E = \frac{A_l \rho_s Y}{k_v \sigma_T^2} \frac{q w_{i,eff}^3}{(UH\chi + U_b H_b)} \left(1 - \frac{q_b}{q_{bc}}\right) \quad (6)$$

where A_l is the cross-sectional area of a sediment grain, k_v is an empirical erodibility constant, σ_T is the tensile strength of the rock, ρ_s is the density of sediment, Y is Young's modulus, q is the volumetric sediment supply per unit width, $w_{i,eff}$ is the effective impact velocity of sediment, U is the streamwise flow velocity, H is the flow depth, χ is an integral relating suspended sediment flux to sediment concentration, flow depth, and velocity, U_b is the streamwise bedload velocity, H_b is the thickness of the bedload layer, q_b is the volumetric bedload flux per unit channel width and q_{bc} is the volumetric bedload transport capacity per unit channel width (Lamb et al., 2008b).

To convert the alluvial bedload flux q_{ba} (calculated from the alluvial reaches) into total sediment supply q , we use a description of the partition of sediment between bedload and suspended load (eq. 20 of Lamb et al., 2008) and solve for q :

$$q = q_{ba} \left(\frac{UH\chi + U_{ba} H_{ba}}{U_{ba} H_{ba}} \right) \quad (7)$$

7.4. Modeling Procedure

We predicted instantaneous incision rates along White Branch Creek using the 1D longitudinal channel profile (sampled at a 100 m interval to remove roughness and noise) and a constant channel width. We used the following procedure to calculate incision rates for each discharge, performing 500,000 iterations for each discharge value:

1. Select value of grain size from uniform distribution.

2. Calculate channel depth in the gorge using 1D energy equation; default to critical depth (eqn. 3) if supercritical flow is predicted.
3. Calculate minimum sediment supply based on shear stress (eqns. 2-4), grain size, slope of alluvium (Fig. 12C), and alluvial channel geometry; this sets the lower bound of the uniform distribution of sediment supply.
4. Select value of sediment supply from uniform distribution; convert to total load sediment supply (eqn. 7).
5. Calculate instantaneous incision rate at each point along the gorge (eqn. 6).
6. Calculate median erosion rate for given parameter set.

8. Combined Role of Large Floods and Annual Discharge

We calculated instantaneous erosion rates for discharges from 1 to 120 m³/s (Figs 16, 17), excluding parameter combinations that resulted in zero erosion. For each discharge, we report the median spatially-averaged incision rate for all model runs. The modeled incision rates are a function of two dimensionless numbers: transport stage (τ^*/τ_{*c}) and relative sediment supply (q_b/q_{bc}) (Sklar and Dietrich, 2004). For a given discharge, transport stage is a function of grain size, while relative sediment supply is a function of both grain size and total sediment supply to the channel. Figure 16 shows the effect of relative sediment supply and transport stage for two modeled discharges: 1 m³/s, approximately representative of annual snowmelt runoff, and 40 m³/s, a representative magnitude for an outburst flood. Unsurprisingly, erosion rates are lower for 1 m³/s than 40 m³/s. There are also fewer combinations of parameters that result in nonzero erosion for 1 m³/s than for 40 m³/s (63 out of 500,000 model runs compared to 12,793/500,000) because the lower shear stress means that the flow is often either below the critical shear

stress for mobilization (transport stage < 1), or cannot transport the full load of sediment (relative sediment supply > 1).

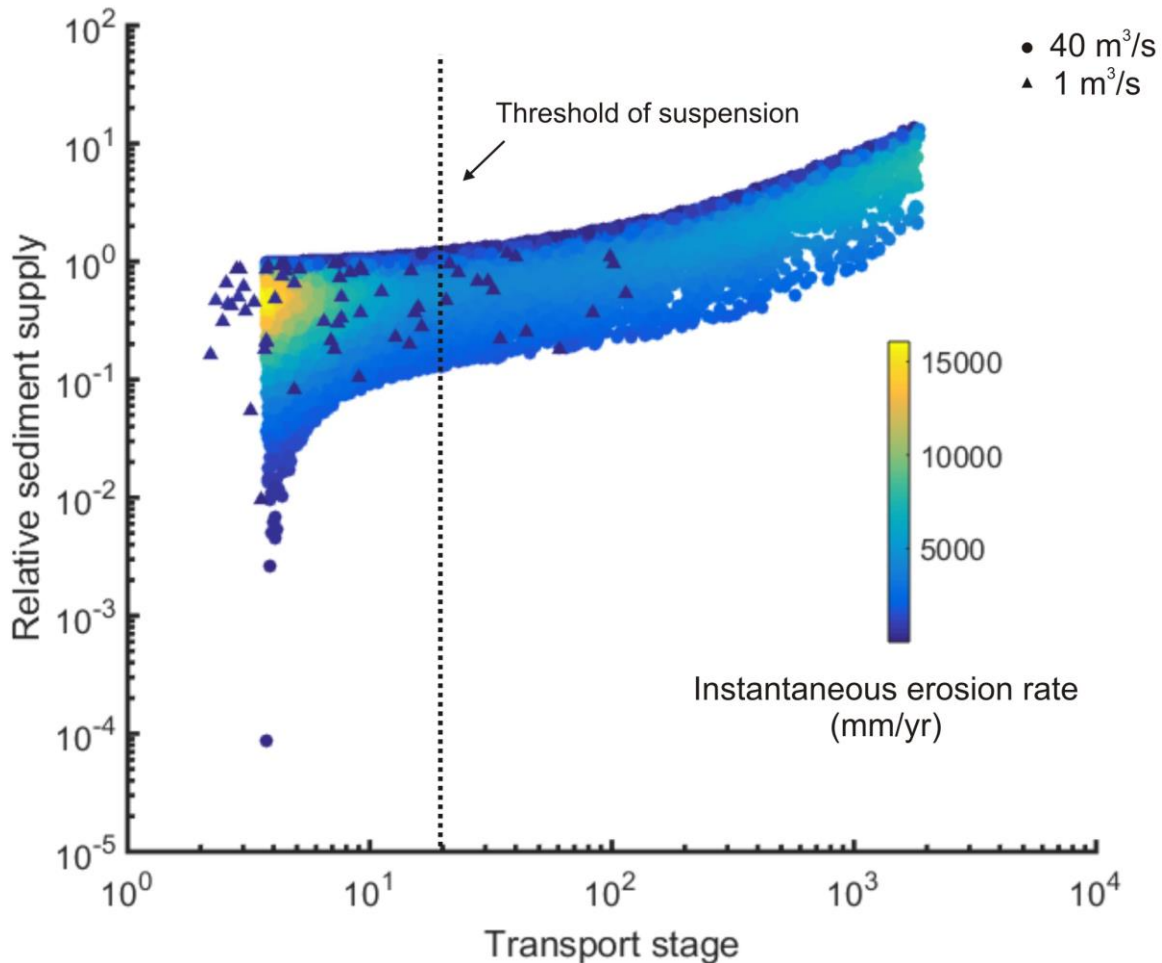


Figure 16. Model behavior. Range of transport stage and relative sediment supply (q_b/q_{bc}) resulting in positive incision for $1 \text{ m}^3/\text{s}$ (triangles) and $40 \text{ m}^3/\text{s}$ (circles), colored by incision rate. The truncated range of transport stages for the $40 \text{ m}^3/\text{s}$ results is due to bounds of input grain size.

Examining the model results for $40 \text{ m}^3/\text{s}$ from low transport stages to high transport stage reveals how incision rate varies within the transport stage-relative sediment supply parameter space. At transport stages much less than the threshold of suspension, most sediment travels as bedload and the highest incision rates occur for

relative sediment supply of ~ 0.5 , similar to the behavior of bedload-only abrasion models (cf. Sklar and Dietrich, 2004). As transport stage increases, hop lengths become longer, causing incision rates to decrease. Near the threshold of suspension, incision rates are nonzero for relative sediment supply values over 1, indicating that suspended sediment is becoming important; when transport stage increases past the threshold of suspension, the higher impact rate due to higher sediment loads causes incision rates to increase again.

Modeled instantaneous incision rates in the gorge reaches of White Branch Creek range from 0.4 to 6 m/yr (Figure 17A). Note that the model predicts unrealistic depths for discharges greater than 70 m³/s (Figure C1) and we exclude these results from our analysis.

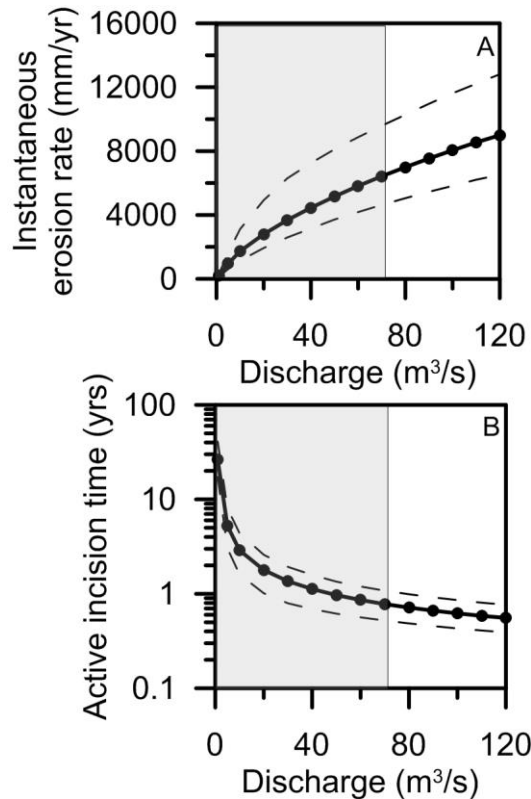


Figure 17. Modeled incision rates and inferred active incision time. A. Median incision rate vs. discharge and B. Inferred time of active incision. Dotted lines show 25th and 75th percentiles. Grey areas demarcate the range of discharges that predict reasonable depths for White Branch Creek.

By dividing total incision in the gorges (~ 5 m) by the average rate for each discharge, we calculated the implied time of active incision (Figure 17B). For the lower end of our discharge range (annual snowmelt), ~ 25 years of continuous incision would be required to form the gorges of White Branch Creek; large events ($40 \text{ m}^3/\text{s}$) would need ~ 1 year continuous incision. Given that we expect typical event duration to be on the order of days for both annual snowmelt and outburst floods, we would need ~9000 snowmelt events or ~360 large floods over 1600 years to carve the channel. The chronology and geology of the area make both of these endmember scenarios unlikely, leading us to conclude that the channel we observe was formed by a combination of outburst floods from Collier Glacier and smaller flows related to annual snowmelt runoff.

9. Discussion/Conclusions

9.1. Incision Mechanisms

We necessarily simplify many aspects of hydraulic and sediment transport dynamics in White Branch Creek, including assumptions of uniform, steady discharge, constant grain size, and constant width. Nevertheless, our results clearly indicate that despite low discharge relative to glacial outburst floods, annual snowmelt flows are capable of doing significant geomorphic work in the channel.

Given that snowmelt runoff is capable of cutting into bedrock, is it possible that outburst floods have no role at all in incision? The presence of abraded obsidian clasts on the lava flow indicates that discharge events passed Obsidian Cliffs (Fig. 9) before traversing the lava flow, strongly suggesting that outburst floods have impacted our study reaches. We confine our modeling to the incision of the coherent core of the lava flow, implicitly assuming that a nascent channel form already existed. The work described in

this paper does not shed light on how this proto-channel initiated, but we speculate that one or more sediment-laden outburst flood events may have “paved” over the permeability of the rubbly surface, enabling surface flow to converge and begin incising. Alternatively, the channel may have initiated via plucking the rubbly surface blocks (e.g., Lamb and Fonstad, 2010), converging to a single channel once the coherent core was exposed. We conclude that while snowmelt runoff may be important once the channel has formed, outburst floods are essential for initiating the onset of fluvial incision in this system.

9.2. Evolution of Temperate Volcanic Landscapes

Megafloods are widely recognized as geomorphic drivers in jointed bedrock, where canyon carving can happen within hours via detaching large blocks from the channel bed. Here, we argue for an intermediate case in which fluvial incision of a blocky lava flow is initiated by an outburst flood(s) from an alpine glacier, and then proceeds through both outburst floods and annual snowmelt runoff. This work has global implications for the timescale of temperate volcanic landscape evolution, where alpine glaciation or large landslides may accelerate fluvial dissection by providing tools and discharge to otherwise sediment-starved systems.

APPENDIX A

SUPPLEMENTAL INFORMATION FOR CHAPTER II

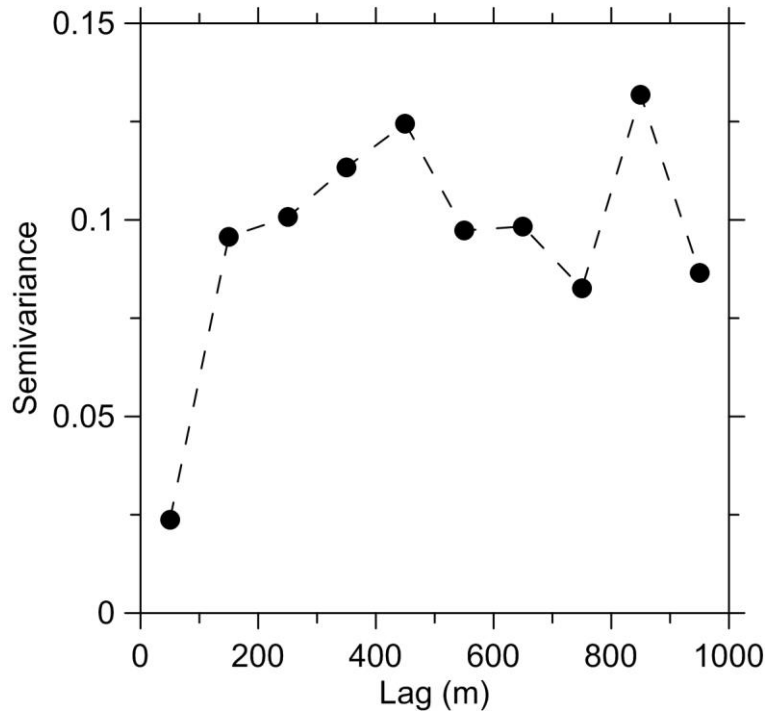


Figure A1. Experimental semi-variogram of HC residence time measurements. Data has been log-transformed and normalized to have a mean of 0. Note that at lags > 100 m, value of semivariance fluctuates around a constant value.

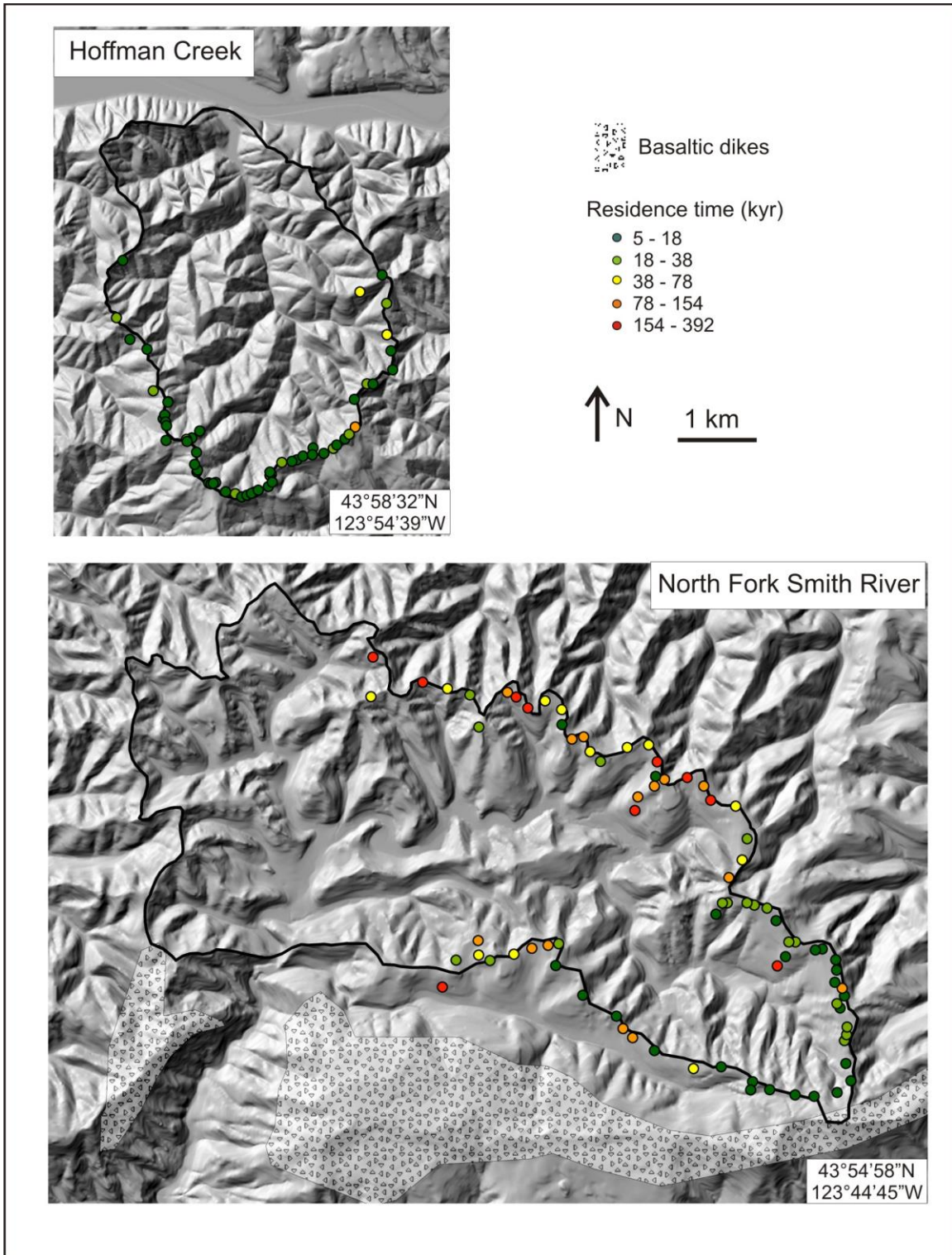


Figure A2. Map of HC and NFSR watersheds with sample locations colored by residence time. Latitude/longitude coordinates are for bottom corner of maps.

APPENDIX B

SUPPLEMENTAL INFORMATION FOR CHAPTER III

Materials and Methods

Steady state of experimental landscapes

We defined flux steady state in our experiments as the point at which the spatially-averaged erosion rate was approximately equal to the imposed rate of baselevel fall (Table B1; Figure B1). To measure erosion rate, we divided the elevation change per pixel (obtained by differencing topographic scans) by the time between scans and then calculated the average value for the entire landscape. The knickpoints visible in the steady-state topography (Fig 6A-E) are related to local accelerated erosion from drop impacts and do not introduce significant transience in our experiments (Figure B2).

Mapping the channel network and channel slope-area analysis

To define the channel network, we must determine both the location of channel heads (e.g., Montgomery and Dietrich, 1989) and how water travels across the landscape surface (Tarboton, 1997). At low drainage areas (hillslopes and colluvial hollows) multidirectional flow algorithms are more representative of natural flow paths (Tarboton, 1997) while at high drainage areas, steepest descent flow routing captures the behavior of flowing water in the channel network (e.g., Wobus et al., 2006). Hence, we defined the channel network using two different approaches: (1) GeoNet, a curvature-based multidirectional channel identification routine (Passalacqua, et al., 2010) to map low-order channels and set the spatial framework for quantifying hillslope metrics (Figure B3A-E) and (2) steepest descent routing to delineate higher order channels for the

advective component (Figure B3F-J). GeoNet includes a Perona-Malik wavelet filter that removes topographic noise while preserving sharp edges common at the hillslope-valley transition (Passalacqua, et al., 2010); we used unfiltered topographic data for the steepest descent flow routing. Because the definition of channel heads in the steepest descent network requires the use of an arbitrary drainage area threshold, our analysis of slope-area scaling in the channel network only considers regions where drainage area is greater than values associated with channel initiation. To find the advective process parameters (see text of Chapter III), we extracted slope and drainage area from the steepest descent network for each experiment and fit a power law to the data using the Matlab nonlinear curve-fitting toolbox.

Mapping hilltops and extracting hillslope metrics

On diffusive hillslopes, disturbance agents (e.g., trees) impart a characteristic scale on the topography that obscures the topographic form associated with long-term continuum sediment transport (Roering et al., 2010). For our experiments, the impacting raindrops dominate topography at the spatial scale of the drop diameter (~3 mm). Hence, before mapping the hilltops in our experiments, we smoothed topography in a moving window using a second-order polynomial fit (Roering et al., 2010; Hurst et al., 2012), setting the diameter of the moving window to the 3 mm diameter of the raindrops. To locate hilltops, we identified areas of the topography with negative curvature, drainage area $< 0.5 \text{ mm}^2$, and slopes $< 1.2 \text{ mm/mm}$ (Roering et al., 2007). We used the hillslope tracing algorithm from Hurst et al. (2012) to calculate average values of hillslope gradient and length for

each experiment, using the GeoNet network (Fig B3A-E) to define the end of hillslope traces.

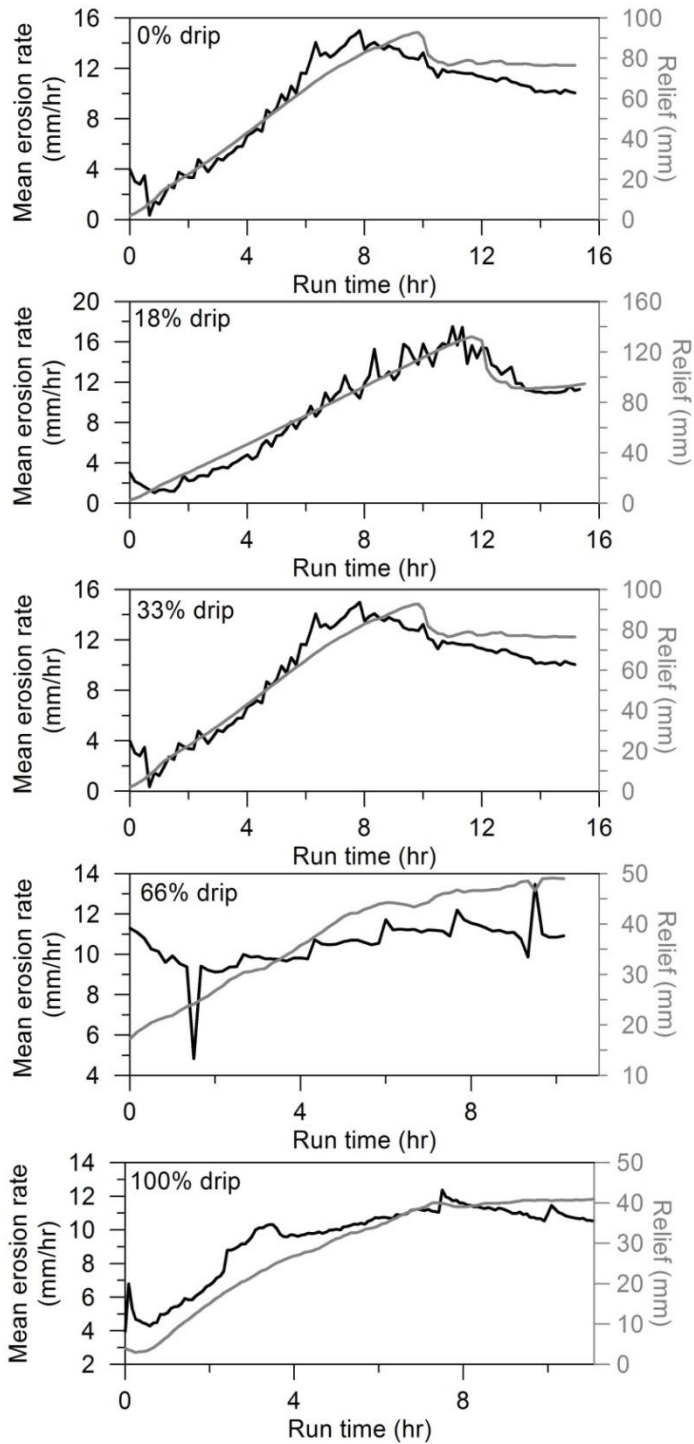


Fig. B1.

Spatially-averaged erosion rate (black) and mean relief of the main divide (grey) for each experiment. Spikes in mean erosion rate of 66% and 100% drip runs are due to priming the drip box; these spikes do not correlate with knickpoints generation and mean erosion rate rapidly returns to its previous value.

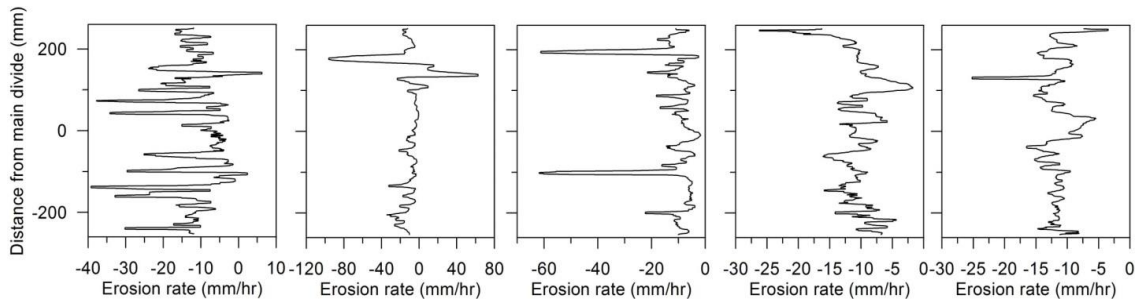


Fig. B2

Average erosion rate calculated over 7.5 mm x 500 mm rectangular moving window oriented parallel to the main divide for all experiments. Large spikes are correlated with knickpoints; the lack of a clear difference in erosion rate between the landscape above and below knickpoints indicates that these features do not result in transient vertical erosion.

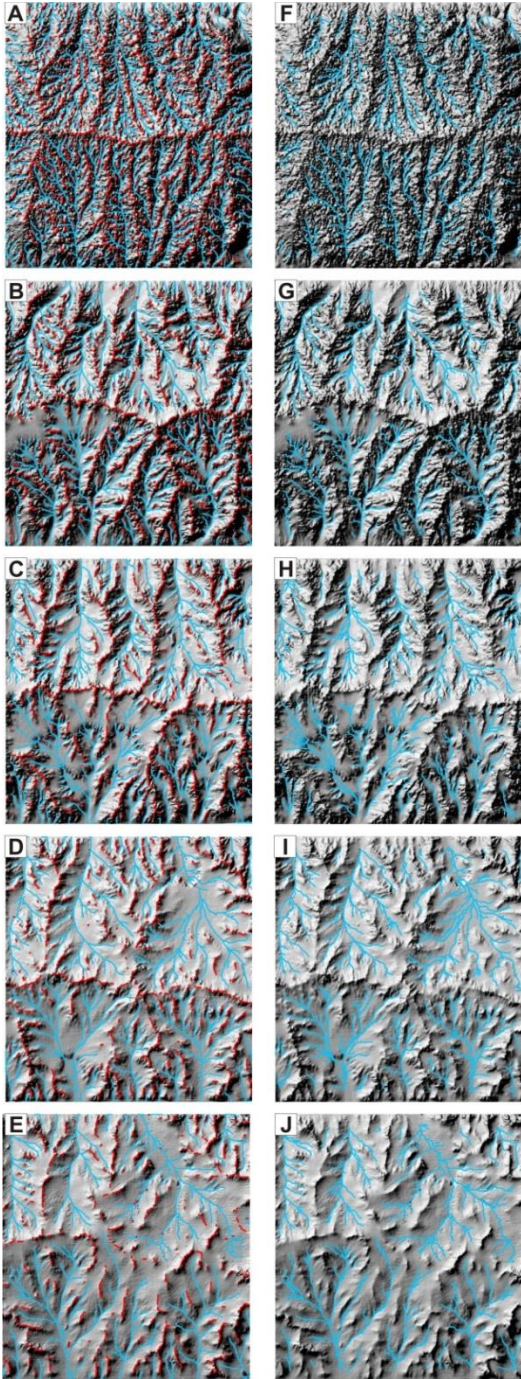


Fig. B3

Hilltop and channel networks; width of topography is 475.5 mm. **A-E** Hillshades of steady-state experimental topography from **A**: 0% drip **B**: 18% drip **C**: 33% drip **D**: 66% drip **E**: 100% drip overlain with GeoNet channel (blue) and hilltop (red) networks. **F-J**: Hillshades of steady-state topography in (**A-E**) overlain with steepest descent networks (blue). Note that the initiation of steepest descent channels is defined solely by a drainage area threshold and should not be taken as an alternative to the curvature-derived GeoNet channel heads.

Table B1.

Experimental variables, topographic metrics, and transport coefficients for steady-state landscapes.

	0% drip	18% drip	33% drip	66% drip	100% drip
Uplift rate (mm/hr)*	11.74	12.11	11.92	11.81	11.46
Rainfall rate (mm/hr)†	38	35.5	33	28	23
Length of drip periods (s/600s)	0	100	200	400	600
Steepness index‡	3.71 ± 1.00	1.76 ± 0.21	0.52 ± 0.1	0.52 ± 0.1	0.6 ± 0.1
Stream power exponent m^{\ddagger}	$0.34 \pm .06$	$0.19 \pm .02$	$0.12 \pm .03$	0.18 ± 0.02	0.21 ± 0.02
Stream power constant $K^{\S,\parallel}$	0.93 ± 0.32	3.41 ± 0.44	15.03 ± 3.25	12.55 ± 2.43	9.76 ± 1.72
Mean hillslope length (mm)[¶]	7.36	13.49	17.73	19.39	22.41
Mean hillslope gradient (mm/mm)[¶]	1.39 ± 0.002	0.99 ± 0.004	0.75 ± 0.005	0.48 ± 0.008	0.37 ± 0.002
Hillslope diffusivity, D (mm² hr⁻¹)^{**}	30.8 ± 4.5	82 ± 6	141 ± 8	238 ± 12.5	345 ± 16
$Pe^{\parallel,\dagger\dagger}$	322.9 ± 233.2	93.9 ± 21.9	104.3 ± 37.9	94.3 ± 31.2	76.57 ± 23.3

* Calculated by differencing initial and final position of sliding weirs and dividing by the total run time.

† Calculated by multiplying the % drip and % mist for each experiment by the discharge from the drip box and mister (23 mm/hr and 38 mm/hr, respectively). For example, rainfall rate for the 18% drip case = $0.18 \cdot 23$ mm/hr + $0.82 \cdot 38$ mm/hr.

‡ Parameters from power-law fit of channel slope-area plots. Parameter uncertainty is from nonlinear least squares fits.

§ Calculated using Eqn. 4 (main text) assuming $n = 1$.

|| Standard error from Gaussian error propagation.

¶ Measured using hillslope tracing algorithm. Uncertainty is +/- standard error.

** Calculated from Eqn. 3 (main text) using iterative procedure, setting S_c to be large (9999). Uncertainty reflects upper and lower bounds of hillslope length and gradient measurements.

†† Calculated from Eqn. 2 (main text).

APPENDIX C

SUPPLEMENTAL INFORMATION FOR CHAPTER IV

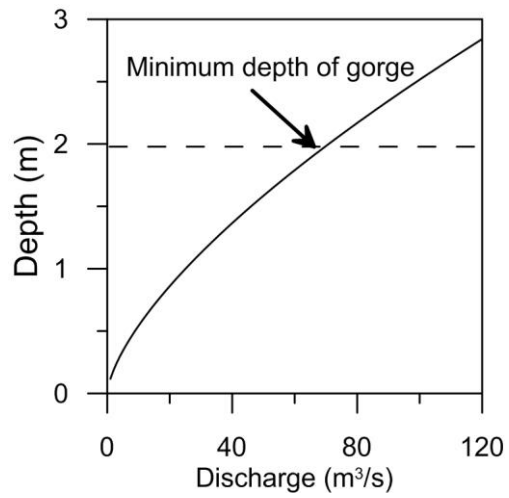


Figure C1. Relationship between critical depth and channel discharge. Dotted line shows minimum depth of gorge, which corresponds to $\sim 70 \text{ m}^3/\text{s}$. Discharges greater than this value produce unreasonable depth values for White Branch Creek.

Table C1. Description of alluvial stratigraphy in upper and lower alluvial deposits on Collier lava flow.

Soil Pit	Location	Depth (cm)	Description
UF 1	E0588324, N4892297	0 - 20	Light brown, silt to fine sand, many fine to medium roots (1 mm - 1cm), some large ~ 2cm diameter roots. Massive, heavily bioturbated by roots. Basal contact is gradual over several cm
		20 - 40	Greyish brown to gray, loose sand and gravel, max clast size 4 cm, massive, not sorted, few fine roots. Basal contact varies, wavy and abrupt. Depth varies to ~ 50 cm across pit.
		40 - 60	Dark gray (almost black) , medium sand, laminated sand with diagonal laminations and some flat laminations. Lenses of fine brown silt up to 2 cm thick, but discontinuous, aligned with laminations. Sharp basal contact.
		60 - 89	Grey brown silt, with many roots. Roots are burned in place but not completely burned. Some specks of detrital charcoal (but could be fine roots?). Laminated in places. Roots are concentrated in upper 10 cm, roots are fine to 1 cm diameter. Abrupt base.
		89 -102	Dark gray fine sand to silt with a few specks fo charcoal. Base is abrupt and is orange-brown color. Weakly laminated, discontinuous. No roots
		106 - 111	Very dark gray to black coarse sand to pea gravel, also coarsens upward, laterally discontinuous throughout pit. Basal contact is gradual. No charcoal.
		111 - 117	Brown to gray brown silt w/ some fine sand, weakly laminated, no charcoal or roots. Gradual basal contact.
		117 - 155	Brown silt, massive, many fine roots and some medium roots (1 cm diameter). Some charcoal, but charcoal could be roots burnt in place. 5 cm or larger rootlet infilled root cast. Sharp base
		155	Top of bedrock

UF 2	E0588274, N4892353	0 - 120	Very coarse imbricated gravel to cobbles. Cobbles up to 20 cm diameter. Very well rounded to rounded. Basal contact is wavy, abrupt, irregular - scour like
		120 - 165	Gray to brown gray silt. Weakly laminated.
		165	Stopped due to safety concerns
UF4	E0588216, N4892264	0 - 10	Brown fill from digging
		10 - 30	Gray brown/brown silt. Massive, heavily bioturbated. Roots common 1 mm - 1cm. Granular silt. Basal contact sharp
		30 - 40	Gray fine pea gravel layer. No sign of imbrication, clast supported, massive. Clasts 1 - 2cm. Basal contact sharp.
		40 - 55	Interbedded very fine sand and silt. Brown silt, weakly laminated, no roots except at base, no charcoal. Interbedded sand and silt. Silt has roots.
		55 -65	Very dark gray to black coarse pea gravel. No large clasts, clasts =< 5 mm. Clast supported and massive. Sharp basal contact.
		65 -68	Brown silt, fine roots. Massive. Sharp basal contact
		68 - 75	Black coarse sand with pea gravel. No roots, no apparent bedding. Looks coarser at bottom - fining upward? Sharp basal contact.
		75 - 97	Very dark gray to brown fine sand and silt with an infilled root cast - root cast filled with pea gravel. No charcoal. Sharp base.
		97 - 119	light to dark gray coarse sand to fine gravel, with 4 cm size rounded clasts. Fine matrix supported, bigger clasts are rare. Sharp basal contact.
		119 - 140	Dark gray to brown laminated silt. Some charcoal flecks concentrated at the top of the deposit.
		140	Top of bedrock. Angular, vesicular clasts.
LF1	E0587204, E4890982	0 - 60	Massive, heavily bioturbated gray brown silt with abundant roots. Basal boundary abrupt.

		60 - 140	Poorly sorted gray to red coarse sand to cobble. Cobbles up to 10 cm diameter. Dominant grain size pea gravel of 2 cm diameter. Clasts are rounded to slightly angular. Few roots. Basal contact is abrupt and linear.
		140-175	Brown to dark gray silt and fine sand with alternating beds at 1 - 5 cm scale. Some fine roots and burned roots in place. Sharp basal contact.
		175-176	Angular red to black gravel; originally identified as bedrock. Paleosol?
		176 - 195	Dark grey to black gravel, clasts up to 5 cm in diameter.
		195	Stopped due to safety concerns
LF2	E0587121, N4891019	0 -20	light gray fine sand and organic material, fine to medium roots, max root diameter 2 cm. Basal contact is gradual over centimeter.
		20 - 40	Laminated fine sand, dark gray to black. Basal contact is wavy and may be bioturbated. Some moderate to fine roots.
		40 - 65	pea gravel to coarse gravel with cobble clasts up to 5 cm. Gray igneous clasts of black to pale gray. Varies considerably in thickness around bit (bioturbation?). Few roots.
		65 - 78	Laminated light gray silt. Basal contact is brown, gradual and organic rich. No charcoal, some root casts.
		78 - 105	Silt massive, fine roots, brown to gray brown, abundant charcoal, a lot of what looks like roots burned in place less of root casts and rotten roots. Basal contact is abrupt.
		105 - 115	Coarse sand, fining upward? Varies in thickness around pit. Laminated in some places, interbedded with fine silt, but this may be bioturbation.
		115 - 147	Very fine silt, very fine roots, banded light gray and brown. Basal contact sharp and wavy.
		147 - 153	Medium sand, basal contact is abrupt. Buried litter layer at base
		153	Pale gray to white; evidence of leaf matter - buried litter layer (Pic 220)
		153 - 182	Weakly laminated fine silt with alternating bands of light gray and brown. Few fine roots.

		182	Stopped due to safety concerns
LF3	E587055, E4891104	0 - 5	Organic litter layer and root mass (roots 1mm - 2 cm). Basal contact is gradual.
		5 - 40	Coarse sand to fine gravel, dark gray, max clast size 2 cm. Clasts are subrounded. Basal contact is abrupt and linear. Very few roots in gravel.
		40 - 55	Laminated sand interbedded at cm scale with gray brown silt. Sparse fine to medium roots, maximum diameter is 2 cm.
		55 - 60	fine sand with occasional cm sized clasts. Friable.
		60 - 75	Firm silt gray to brown. Moderate fine roots and charcoal. Massive.
		75 - 82	Gray to brown silt interbedded with fine black sand, sand is looser than the silt.
		82 - 90	fine to medium black sand, weakly laminated. Basal contact is wavy and sharp.
		90 - 101	very loose gravel to cobble with some fine sand. At same level, fine sand and silt; boundary ambiguous. Gravel is more continuous around pit while silt and sand appears to be only in one place.
		101 - 145	Alternating layers of brown silt with root casts and gray fine sand. Boundaries are diffuse. Basal contact is sharp. Charcoal present.
		145 - 152	Subrounded gravel, clasts up to 4 cm. Finer than above gravel layer. No roots. Basal contact sharp and wavy.
		152 - 182	Alternating layers of brown silt with root casts and gray fine sand. Boundaries are diffuse. Basal contact is sharp.
		182 - 195	Coarse gravel to cobble; max clast diameter 4 cm. No roots.
		195	Stopped due to safety concerns

Table C2. Constant parameter values for bedrock incision modeling in Chapter IV

Symbol	Description	Value used
w_a	Width of alluvial channel	11 m
w_g	Width of bedrock gorge	8 m
τ_c	critical shields stress for incipient motion (dimensionless)	0.04
ρ_s	sediment density	2650 kg m ⁻³
ρ_w	water density	1000 kg m ⁻³
γ	Young's modulus	5 x 10 ¹⁰ Pa
k_v	empirical bedrock erodibility coefficient (dimensionless)	1.00E+06
σ_T	rock tensile strength	7 x 10 ⁶ Pa
R	specific density of sediment (dimensionless): 1.65	1.65
g	acceleration of gravity	9.8 m·s ⁻²

REFERENCES CITED

Chapter II

- Almond, P., Roering, J., and Hales, T.C., 2007, Using soil residence time to delineate spatial and temporal patterns of transient landscape response: *Journal of Geophysical Research*, v. 112, no. F3, doi:10.1029/2006JF000568.
- Birkeland, P.W., 1999, *Soils and Geomorphology*: Oxford, UK, Oxford University Press
- Clark, R.N., and Roush, T.L., 1984, Reflectance spectroscopy: Quantitative analysis Techniques for remote sensing applications: *Journal of Geophysical Research*, v. 89, no. B7, p. 6329–6340, doi:10.1029/JB089iB07p06329.
- Fernandes, N.F., and Dietrich, W.E., 1997, Hillslope evolution by diffusive processes: The timescale for equilibrium adjustments: *Water Resources Research*, v. 33, no. 6, p. 1307–1318, doi:10.1029/97WR00534.
- Gabet, E.J., 2000, Gopher bioturbation: field evidence for non-linear hillslope diffusion: *Earth Surface Processes and Landforms*, v. 25, no. 13, p. 1419–1428, doi:10.1002/1096-9837(200012)25:13<1419::AID-ESP148>3.0.CO;2-1.
- Gabet, E.J., and Mudd, S.M., 2010, Bedrock erosion by root fracture and tree throw: A coupled biogeomorphic model to explore the humped soil production function and the persistence of hillslope soils: *Journal of Geophysical Research*, v. 115, no. F4, p. 1–14, doi:10.1029/2009JF001526.
- Hasbargen, L., and Paola, C., 2000, Landscape instability in an experimental drainage basin: *Geology*, doi:10.1130/0091-7613(2000)28<1067:LIIAED>2.0.CO;2.
- Heimsath, A.M., Dietrich, W.E., Nishiizumi, K., and Finkel, R.C., 2001, Stochastic processes of soil production and transport: Erosion rates, topographic variation and cosmogenic nuclides in the Oregon Coast Range: *Earth Surface Processes and Landforms*, v. 26, no. 5, p. 531–552, doi:10.1002/esp.209.
- Heller, P.L., and Dickinson, W.R., 1985, Submarine ramp facies model for delta-fed, sand-rich turbidite systems: *The American Association of Petroleum Geologists Bulletin*, v. 69, no. 6, p. 960.
- Jenny, H., 1941, *Factors of Soil Formation: A System of Quantitative Pedology*: New York, McGraw Hill.
- Lague, D., 2003, Laboratory experiments simulating the geomorphic response to tectonic uplift: *Journal of Geophysical Research*, v. 108, no. B1, doi:10.1029/2002JB001785.

- McFadden, L.D., and Hendricks, D.M., 1985, Changes in the content and composition of pedogenic iron oxyhydroxides in a chronosequence of soils in southern California: *Quaternary Research*, v. 23, no. 2, p. 189–204, doi:10.1016/0033-5894(85)90028-6.
- Meigs, A., Brozovic, N., and Johnson, M.L., 1999, Steady, balanced rates of uplift and erosion of the Santa Monica Mountains, California: *Basin Research*, v. 11, no. 1, p. 59–73, doi:10.1046/j.1365-2117.1999.00083.x.
- Mudd, S.M., and Furbish, D.J., 2005, Lateral migration of hillcrests in response to channel incision in soil-mantled landscapes: *Journal of Geophysical Research*, v. 110, no. F4, p. 1–18, doi:10.1029/2005JF000313.
- Mudd, S.M., and Yoo, K., 2010, Reservoir theory for studying the geochemical evolution of soils: *Journal of Geophysical Research*, v. 115, no. F3, p. 1–13, doi:10.1029/2009JF001591.
- Norton, D.A., 1989, Tree windthrow and forest soil turnover: *Canadian Journal of Forest Research*, v. 19, p. 386–389, doi:10.1139/x89-059.
- Patching, W.R., 1987, *Soil Survey of Lane County Area, Oregon*: 369 p.
- Pelletier, J.D., 2004, Persistent drainage migration in a numerical landscape evolution model: *Geophysical Research Letters*, v. 31, no. 20, p. 4–7, doi:10.1029/2004GL020802.
- Perron, J.T., Kirchner, J.W., and Dietrich, W.E., 2009, Formation of evenly spaced ridges and valleys: *Nature*, v. 460, no. 7254, p. 502–505, doi:10.1038/nature08174.
- Personius, S.F., 1995, Late Quaternary stream incision and uplift in the forearc of the Cascadia subduction zone, western Oregon: p. 20193–20210.
- Reneau, S.L., and Dietrich, W.E., 1991, Erosion rates in the southern Oregon coast range: Evidence for an equilibrium between hillslope erosion and sediment yield: *Earth Surface Processes and Landforms*, v. 16, no. 4, p. 307–322, doi:10.1002/esp.3290160405.
- Riebe, C.S., Kirchner, J.W., and Finkel, R.C., 2004, Erosional and climatic effects on long-term chemical weathering rates in granitic landscapes spanning diverse climate regimes: *Earth and Planetary Science Letters*, v. 224, no. 3–4, p. 547–562, doi:10.1016/j.epsl.2004.05.019.
- Rinaldo, A., Dietrich, W.E., Rigon, R., Vogel, G.K., and Rodriguez-Iturbe, I., 1995, Geomorphological signatures of varying climate: *Nature*, v. 374, no. 6523, p. 632–635, doi:10.1038/374632a0.

Roering, J.J., Marshall, J., Booth, A.M., Mort, M., and Jin, Q., 2010, Evidence for biotic controls on topography and soil production: *Earth and Planetary Science Letters*, v. 298, no. 1–2, p. 183–190, doi:10.1016/j.epsl.2010.07.040.

Scheinost, C., 1998, Use and limitations of second-derivative diffuse reflectance spectroscopy in the visible to near-infrared range to identify and quantify Fe oxide minerals in soils: *Clays and Clay Minerals*, v. 46, no. 5, p. 528–536, doi:10.1346/CCMN.1998.0460506.

Schwertmann, U., and Taylor, R.M., 1989, Iron oxides, in Dixon, J.B., and Weed, S.B., eds., *Minerals in Soil Environments*: Madison, Wisconsin, Soil Science Society of America, p. 379–438.

Stock, J., and Dietrich, W.E., 2003, Valley incision by debris flows: Evidence of a topographic signature: *Water Resources Research*, v. 39, no. 4, doi:10.1029/2001WR001057.

Viscarra Rossel, R.a., Bui, E.N., de Caritat, P., and McKenzie, N.J., 2010, Mapping iron oxides and the color of Australian soil using visible–near-infrared reflectance spectra: *Journal of Geophysical Research*, v. 115, no. F4, p. 1–13, doi:10.1029/2009JF001645.

Willett, S.D., and Brandon, M.T., 2002, On steady states in mountain belts: *Geology*, doi:10.1130/0091-7613(2002)030<0175:OSSIMB>2.0.CO;2.

Chapter III

Bonnet, S., 2009, Shrinking and splitting of drainage basins in orogenic landscapes from the migration of the main drainage divide: *Nature Geoscience*, v. 2, no. 11, p. 766–771, doi: 10.1038/ngeo666.

Bonnet, S., and Crave, A., 2003, Landscape response to climate change : Insights from experimental modeling and implications for tectonic versus climatic uplift of topography: *Geology*, doi: 10.1130/0091-7613(2003)031<0123.

Chadwick, O. a., Roering, J.J., Heimsath, A.M., Levick, S.R., Asner, G.P., and Khomo, L., 2013, Shaping post-orogenic landscapes by climate and chemical weathering: *Geology*, v. 41, no. 11, p. 1171–1174, doi: 10.1130/G34721.1.

Davis, W., 1892, The convex profile of badland divides: *Science (New York, NY)*, v. 20, no. 508, p. 245.

Dietrich, W., Wilson, C., and Montgomery, D., 1992, Erosion thresholds and land surface morphology: *Geology*, v. 20, p. 675–679, doi: 10.1130/0091-7613(1992)020<0675.

- Dixon, J.L., Heimsath, A.M., Kaste, J., and Amundson, R., 2009, Climate-driven processes of hillslope weathering: *Geology*, v. 37, no. 11, p. 975–978, doi: 10.1130/G30045A.1.
- Furbish, D.J., Hamner, K.K., and Schmeeckle, M.W., 2007, Rain splash of dry sand revealed by high-speed imaging and sticky paper splash targets: *Journal of Geophysical Research*, v. 112, no. F1.
- Gabet, E.J., 2000, Gopher bioturbation: field evidence for non-linear hillslope diffusion: *Earth Surface Processes and Landforms*, v. 25, no. 13, p. 1419–1428, doi: 10.1002/1096-9837(200012)25:13<1419::AID-ESP148>3.0.CO;2-1.
- Gilbert, G.K., 1909, The convexity of hilltops: *The Journal of Geology*, v. 17, no. 4, p. 344–350.
- Hasbargen, L., and Paola, C., 2000, Landscape instability in an experimental drainage basin: *Geology*, doi: 10.1130/0091-7613(2000)28<1067.
- Horton, R., 1945, Erosional development of streams and their drainage basins; hydrophysical approach to quantitative morphology: *Geological Society of America Bulletin*, v. 56, no. 3, p. 275–370, doi: 10.1130/0016-7606(1945)56.
- Howard, A.D., 1994, A detachment-limited model of drainage basin evolution: *Water Resources Research*, v. 30, no. 7, p. 2261–2286.
- Hurst, M.D., Mudd, S.M., Walcott, R., Attal, M., and Yoo, K., 2012, Using hilltop curvature to derive the spatial distribution of erosion rates: *Journal of Geophysical Research*, v. 117, no. F2, p. 1–19, doi: 10.1029/2011JF002057.
- Kirkby, M.J., 1971, Hillslope process-response models based on the continuity equation: *Special Publication, Institute of British Geographers*, v. 3, p. 15–30.
- Lague, D., Crave, A., and Davy, P., 2003, Laboratory experiments simulating the geomorphic response to tectonic uplift: *Journal of Geophysical Research*, v. 108, no. B1, doi: 10.1029/2002JB001785.
- Matsuoka, N., 1998, The Relationship between Frost Heave and Downslope Soil Movement : Field Measurements in the Japanese Alps: *Permafrost and Periglacial Processes*, v. 133, no. January, p. 121–133.
- Moglen, G., Eltahir, E., and Bras, R., 1998, On the sensitivity of drainage density to climate change: *Water Resources Research*, v. 34, no. 4, p. 855–862.
- Montgomery, D., and Dietrich, W., 1989, Source areas, drainage density, and channel initiation: *Water Resources Research*, v. 25, no. 8, p. 1907–1918.

- Paola, C., Straub, K., Mohrig, D., and Reinhardt, L., 2009, The “unreasonable effectiveness” of stratigraphic and geomorphic experiments: *Earth-Science Reviews*, v. 97, no. 1-4, p. 1–43, doi: 10.1016/j.earscirev.2009.05.003.
- Passalacqua, P., Do Trung, T., Fofoula-Georgiou, E., Sapiro, G., and Dietrich, W.E., 2010, A geometric framework for channel network extraction from lidar: Nonlinear diffusion and geodesic paths: *Journal of Geophysical Research*, v. 115, no. F1, p. F01002, doi: 10.1029/2009JF001254.
- Perron, J.T., Dietrich, W.E., and Kirchner, J.W., 2008, Controls on the spacing of first-order valleys: *Journal of Geophysical Research*, v. 113, no. F4, p. 1–21, doi: 10.1029/2007JF000977.
- Perron, J.T., Kirchner, J.W., and Dietrich, W.E., 2009, Formation of evenly spaced ridges and valleys: *Nature*, v. 460, no. 7254, p. 502–505, doi: 10.1038/nature08174.
- Rinaldo, A., Dietrich, W.E., Rigon, R., Vogel, G.K., and Rodriguez-Iturbe, I., 1995, Geomorphological signatures of varying climate: *Nature*, v. 374, no. 6523, p. 632–635, doi: 10.1038/374632a0.
- Roering, J.J., Kirchner, J.W., and Dietrich, W.E., 2001, Hillslope evolution by nonlinear, slope-dependent transport: Steady state morphology and equilibrium adjustment timescales: *Journal of Geophysical Research*, v. 106, no. B8, p. 16499–16513.
- Roering, J.J., Marshall, J., Booth, A.M., Mort, M., and Jin, Q., 2010, Evidence for biotic controls on topography and soil production: *Earth and Planetary Science Letters*, v. 298, no. 1-2, p. 183–190, doi: 10.1016/j.epsl.2010.07.040.
- Roering, J.J., Perron, J.T., and Kirchner, J.W., 2007, Functional relationships between denudation and hillslope form and relief: *Earth and Planetary Science Letters*, v. 264, no. 1-2, p. 245–258, doi: 10.1016/j.epsl.2007.09.035.
- Smith, T.R., and Bretherton, F.P., 1972, Stability and the conservation of mass in drainage basin evolution: *Water Resources Research*, v. 8, no. 6, p. 1506–1529.
- Stock, J., and Dietrich, W.E., 2003, Valley incision by debris flows: Evidence of a topographic signature: *Water Resources Research*, v. 39, no. 4, doi: 10.1029/2001WR001057.
- Taylor Perron, J., and Fagherazzi, S., 2012, The legacy of initial conditions in landscape evolution: *Earth Surface Processes and Landforms*, v. 37, no. 1, p. 52–63, doi: 10.1002/esp.2205.
- Tucker, G.E., and Slingerland, R., 1997, Drainage basin responses to climate change: *Water Resources Research*, v. 33, no. 8, p. 2031–2047.

Turowski, J.M., Lague, D., Crave, A., and Hovius, N., 2006, Experimental channel response to tectonic uplift: *Journal of Geophysical Research*, v. 111, no. F3, p. 1–12, doi: 10.1029/2005JF000306.

Whipple, K., and Tucker, G.E., 1999, Dynamics of the stream-power river incision model: Implications for height limits of mountain ranges, landscape response timescales, and research needs: *Journal of Geophysical Research*, v. 104, p. 661–674.

Wobus, C., Whipple, K., Kirby, E., Snyder, N.P., Johnson, J.P.L., Spyropolou, K., Crosby, B., and Sheehan, D., 2006, Tectonics from topography: Procedures, promise, and pitfalls, in Willett, S.D., Hovius, N., Brandon, M.T., and Fisher, D.M. eds., *Tectonics, Climate, and Landscape Evolution: Geological Society of America Special Paper 398*, p. 55–74.

Chapter IV

Baynes, E.R.C., Attal, M., Niedermann, S., Kirstein, L. a., Dugmore, A.J., and Naylor, M., 2015, Erosion during extreme flood events dominates Holocene canyon evolution in northeast Iceland: *Proceedings of the National Academy of Sciences*, v. 112, no. 8, p. 201415443, doi: 10.1073/pnas.1415443112.

Bronk Ramsey, C., 2009, Bayesian Analysis of Radiocarbon Dates: *Radiocarbon*, v. 51, no. 1, p. 337–360, doi: 10.2458/azu_js_rc.v51i1.3494.

Chatanantavet, P., and Parker, G., 2009, Physically based modeling of bedrock incision by abrasion, plucking, and macroabrasion: *Journal of Geophysical Research*, v. 114, no. F4, p. 1–22, doi: 10.1029/2008JF001044.

Collinson, J., Mountney, N., and Thompson, D., 2006, *Sedimentary Structures: Third Edition*: Dunedin Academic Press, Dunedin, United Kingdom.

Cook, K.L., Turowski, J.M., and Hovius, N., 2013, A demonstration of the importance of bedload transport for fluvial bedrock erosion and knickpoint propagation: *Earth Surface Processes and Landforms*, v. 38, no. 7, p. 683–695, doi: 10.1002/esp.3313.

Deardorff, N.D., and Cashman, K. V., 2012, Emplacement conditions of the c. 1,600-year bp Collier Cone lava flow, Oregon: A LiDAR investigation: *Bulletin of Volcanology*, v. 74, no. 9, p. 2051–2066, doi: 10.1007/s00445-012-0650-9.

Deligne, N.I., Cashman, K. V., and Roering, J.J., 2013, After the lava flow: The importance of external soil sources for plant colonization of recent lava flows in the central Oregon Cascades, USA: *Geomorphology*, v. 202, p. 15–32, doi: 10.1016/j.geomorph.2012.12.009.

- Fernandez Luque, R., and Van Beek, R., 1976, Erosion And Transport Of Bed-Load Sediment: *Journal of Hydraulic Research*, v. 14, no. 2, p. 127–144, doi: 10.1080/00221687609499677.
- Ferrier, K.L., Huppert, K.L., and Perron, J.T., 2013, Climatic control of bedrock river incision.: *Nature*, v. 496, no. 7444, p. 206–9, doi: 10.1038/nature11982.
- Freeze, R.A., and Cherry, J.A., 1979, *Groundwater*: Prentice Hall, Englewood Cliffs, NJ.
- Gilbert, G.K., 1877, *Report on the Geology of the Henry Mountains*: U.S. Geological Survey
- Gran, K.B., and Montgomery, D.R., 2005, Spatial and temporal patterns in fluvial recovery following volcanic eruptions: Channel response to basin-wide sediment loading at Mount Pinatubo, Philippines: *Bulletin of the Geological Society of America*, v. 117, no. 1-2, p. 195–211, doi: 10.1130/B25528.1.
- Hobley, D.E.J., Sinclair, H.D., Mudd, S.M., and Cowie, P. a., 2011, Field calibration of sediment flux dependent river incision: *Journal of Geophysical Research*, v. 116, no. F4, p. 1–18, doi: 10.1029/2010JF001935.
- Hopson, R.E., 1960, Collier Glacier - a photographic record: *Mazama*, v. 42, no. 13, p. 37 – 39.
- Howard, A.D., 1994, A detachment-limited model of drainage basin evolution: *Water resources research*, v. 30, no. 7, p. 2261–2286.
- Jefferson, A., Ferrier, K., Perron, J.T., and Ramalho, R., 2014, Controls on the Hydrological and Topographic Evolution of Shield Volcanoes and Volcanic Ocean Islands, in Harpp, K.S., Mittelstaedt, E., D'Ozouville, N., and Graham, D.W. eds., *The Galápagos: A Natural Laboratory for the Earth Sciences*, American Geophysical Union.
- Jefferson, A., Grant, G.E., Lewis, S.L., and Lancaster, S.T., 2010, Coevolution of hydrology and topography on a basalt landscape in the Oregon Cascade Range, USA: *Earth Surface Processes and Landforms*, v. 35, no. January, p. 803–816, doi: 10.1002/esp.1976.
- Johnson, J.P.L., Whipple, K.X., Sklar, L.S., and Hanks, T.C., 2009, Transport slopes, sediment cover, and bedrock channel incision in the Henry Mountains, Utah: *Journal of Geophysical Research*, v. 114, no. F2, p. 1–21, doi: 10.1029/2007JF000862.
- Kilburn, C.R., 2000, Lava flows and flow fields, in Sigurdsson, H., Houghton, B.F., McNutt, S.R., Rymer, H., and Stix, J. eds., *Encyclopedia of Volcanoes*, Academic

- Press, San Diego, CA, p. 291 – 305.
- Lamb, M.P., and Dietrich, W.E., 2009, The persistence of waterfalls in fractured rock: *Bulletin of the Geological Society of America*, v. 121, no. 7-8, p. 1123–1134, doi: 10.1130/B26482.1.
- Lamb, M.P., Dietrich, W.E., Aciego, S.M., Depaolo, D.J., and Manga, M., 2008a, Formation of Box Canyon, Idaho, by megaflood: implications for seepage erosion on Earth and Mars.: *Science (New York, N.Y.)*, v. 320, no. 5879, p. 1067–1070, doi: 10.1126/science.1156630.
- Lamb, M.P., Dietrich, W.E., and Sklar, L.S., 2008b, A model for fluvial bedrock incision by impacting suspended and bed load sediment: *Journal of Geophysical Research*, v. 113, no. F3, p. 1–18, doi: 10.1029/2007JF000915.
- Lamb, M.P., and Fonstad, M. a., 2010, Rapid formation of a modern bedrock canyon by a single flood event: *Nature Geoscience*, v. 3, no. 7, p. 477–481, doi: 10.1038/ngeo894.
- Lamb, M.P., Mackey, B.H., and Farley, K. a, 2014, Amphitheater-headed canyons formed by megaflooding at Malad Gorge, Idaho: *Proceedings of the National Academy of Sciences of the United States of America*, v. 111, no. 1, p. 57–62, doi: 10.1073/pnas.1312251111.
- Lohse, K. a., and Dietrich, W.E., 2005, Contrasting effects of soil development on hydrological properties and flow paths: *Water Resources Research*, v. 41, no. 12, p. 1–17, doi: 10.1029/2004WR003403.
- Mackin, J.H., 1948, Concept of the graded river: *Geological Society of America Bulletin*, v. 101, p. 1373–1388.
- Major, J., Pierson, T., Dinehart, R., and Costa, J., 2000, Sediment yield following severe volcanic disturbance—a two-decade perspective from Mount St. Helens: *Geology*, , no. 9, p. 819–822.
- Marcott, S. a., Fountain, A.G., O’Connor, J.E., Sniffen, P.J., and Dethier, D.P., 2009, A latest Pleistocene and Holocene glacial history and paleoclimate reconstruction at Three Sisters and Broken Top Volcanoes, Oregon, U.S.A.: *Quaternary Research*, v. 71, no. 2, p. 181–189, doi: 10.1016/j.yqres.2008.09.002.
- Montgomery, D.R., 2001, Slope distributions, threshold hillslopes, and steady-state topography: *American Journal of Science*, v. 301, no. 4-5, p. 432–454, doi: 10.2475/ajs.301.4-5.432.
- Montgomery, D.R., and Buffington, J.M., 1997, Channel-reach morphology in mountain drainage basins: *Geological Society Of America Bulletin*, doi: 10.1130/0016-7606(1997)109<0596.

- O'Connor, J.E., and Costa, J.E., 2008, The World's Largest Floods, Past and Present – Their Causes and Magnitudes: U.S. Geological Survey Circular 1254:.
- O'Connor, J.E., Hardison, J.H., and Costa, J.E., 2001, Debris flows from failures Neoglacial-age moraine dams in the Three Sisters and Mount Jefferson wilderness areas: U.S. Geological Survey Professional Paper.
- Parker, G., 1978, Self-formed straight rivers with equilibrium banks and mobile bed. Part 2. The gravel river: *Journal of Fluid Mechanics*, v. 89, no. 01, p. 127, doi: 10.1017/S0022112078002505.
- Scheingross, J.S., Brun, F., Lo, D.Y., Omerdin, K., and Lamb, M.P., 2014, Experimental evidence for fluvial bedrock incision by suspended and bedload sediment: *Geology*, v. 42, no. 6, p. 523–526, doi: 10.1130/G35432.1.
- Sherrod, D.R., Taylor, E.M., Ferns, M.L., Scott, W.E., Conrey, R.M., and Smith, G. a., 2004, Geologic Investigations Series - Geologic map of the Bend 30- X 60-minute quadrangle, central Oregon:.
- Sklar, L.S., and Dietrich, W.E., 2004, A mechanistic model for river incision into bedrock by saltating bed load: *Water Resources Research*, v. 40, no. 6, p. 1–22, doi: 10.1029/2003WR002496.
- Sklar, L.S., and Dietrich, W.E., 2001, Sediment and rock strength controls on river incision into bedrock: *Geology*, v. 29, no. 12, p. 1087–1090, doi: 10.1130/0091-7613(2001)029<1087:SARSCO>2.0.CO.
- Sklar, L.S., and Dietrich, W.E., 2006, The role of sediment in controlling steady-state bedrock channel slope: Implications of the saltation–abrasion incision model: *Geomorphology*, v. 82, no. 1-2, p. 58–83, doi: 10.1016/j.geomorph.2005.08.019.
- Stock, J.D., Schmidt, K.M., and Miller, D.M., 2008, Controls on alluvial fan long-profiles: *Bulletin of the Geological Society of America*, v. 120, no. 5-6, p. 619–640, doi: 10.1130/B26208.1.
- Swanson, F.J., Jones, J. a., Crisafulli, C.M., and Lara, A., 2013, Effects of volcanic and hydrologic processes on forest vegetation: Chaitén Volcano, Chile: *Andean Geology*, v. 40, no. 2, p. 359–391, doi: 10.5027/andgeoV40n2-a10.
- Turowski, J.M., Lague, D., and Hovius, N., 2007, Cover effect in bedrock abrasion: A new derivation and its implications for the modeling of bedrock channel morphology: *Journal of Geophysical Research*, v. 112, no. F4, p. 1–16, doi: 10.1029/2006JF000697.

- Turowski, J.M., and Rickenmann, D., 2009, Tools and cover effects in bedload transport observations in the Pitzbach, Austria: *Earth Surface Processes and Landforms*, v. 34, p. 27–37, doi: 10.1002/esp.1686.
- Whipple, K.X., Hancock, G.S., and Anderson, R.S., 2000a, River incision into bedrock: Mechanics and relative efficacy of plucking, abrasion, and cavitation: *Geological Society of America Bulletin*, v. 112, no. 3, p. 490, doi: 10.1130/0016-7606(2000)112<490:RIIBMA>2.0.CO;2.
- Whipple, K.X., Snyder, N.P., and Dollenmayer, K., 2000b, Rates and processes of bedrock incision by the Upper Ukak River since the 1912 Novarupta ash flow in the Valley of Ten Thousand Smokes , Alaska: *Geology* , no. 9, p. 835–838.
- Wobus, C., Whipple, K., Kirby, E., Snyder, N.P., Johnson, J.P.L., Spyropolou, K., Crosby, B., and Sheehan, D., 2006, Tectonics from topography: Procedures, promise, and pitfalls, in Willett, S.D., Hovius, N., Brandon, M.T., and Fisher, D.M. eds., *Tectonics, Climate, and Landscape Evolution: Geological Society of America Special Paper 398*, p. 55–74.
- Wohl, E.E., 2000, Channel Processes, in *Mountain Rivers*, American Geophysical Union, Washington, D.C.
- Wohl, E.E., and Merritt, D.M., 2001, Bedrock channel morphology: *Geological Society Of America Bulletin*, doi: 10.1130/0016-7606(2001)113<1205.
- Wolman, M.G., and Miller, J.P., 1960, Magnitude and Frequency of Forces in Geomorphic Processes: *The Journal of Geology*, v. 68, no. 1, p. 54–74, doi: 10.1086/626637.